

Global Magnetohydrodynamic Magnetosphere Simulation With an Adaptively Embedded Particle-In-Cell Model

Xiantong Wang¹ , Yuxi Chen^{1,2} , and Gábor Tóth¹ 

¹Department of Climate and Space Sciences and Engineering, University of Michigan, Ann Arbor, MI, USA, ²Now at Princeton Plasma Physics Laboratory, Princeton University, Princeton, NJ, USA

Key Points:

- We perform a global simulation of a geomagnetic storm event with kinetic modeling of the magnetotail reconnection
- The kinetic region is adaptively embedded to the magnetohydrodynamic model and the reconnection sites are identified by physical criteria during the runtime
- The global scale, mesoscale, and electron scale features are observed simultaneously in one simulation

Correspondence to:

X. Wang,
xtwang@umich.edu

Citation:

Wang, X., Chen, Y., & Tóth, G. (2022). Global magnetohydrodynamic magnetosphere simulation with an adaptively embedded particle-in-cell model. *Journal of Geophysical Research: Space Physics*, 127, e2021JA030091. <https://doi.org/10.1029/2021JA030091>

Received 1 NOV 2021
Accepted 12 AUG 2022

Author Contributions:

Conceptualization: Xiantong Wang, Yuxi Chen, Gábor Tóth
Formal analysis: Xiantong Wang
Funding acquisition: Gábor Tóth
Investigation: Xiantong Wang
Methodology: Xiantong Wang, Yuxi Chen, Gábor Tóth
Project Administration: Gábor Tóth
Software: Xiantong Wang
Supervision: Gábor Tóth
Validation: Xiantong Wang
Visualization: Xiantong Wang
Writing – original draft: Xiantong Wang
Writing – review & editing: Yuxi Chen, Gábor Tóth

Abstract We perform a geomagnetic event simulation using a newly developed magnetohydrodynamic with adaptively embedded particle-in-cell (MHD-AEPIC) model. We have developed effective criteria to identify reconnection sites in the magnetotail and cover them with the PIC model. The MHD-AEPIC simulation results are compared with Hall MHD and ideal MHD simulations to study the impacts of kinetic reconnection at multiple physical scales. At the global scale, the three models produce very similar SYM-H and SuperMag Electrojet indexes, which indicates that the global magnetic field configurations from the three models are very close to each other. We also compare the ionospheric solver results and all three models generate similar polar cap potentials and field-aligned currents. At the mesoscale, we compare the simulations with in situ Geotail observations in the tail. All three models produce reasonable agreement with the Geotail observations. At the kinetic scales, the MHD-AEPIC simulation can produce a crescent shape distribution of the electron velocity space at the electron diffusion region, which agrees very well with MMS observations near a tail reconnection site. These electron scale kinetic features are not available in either the Hall MHD or ideal MHD models. Overall, the MHD-AEPIC model compares well with observations at all scales, it works robustly, and the computational cost is acceptable due to the adaptive adjustment of the PIC domain. It remains to be determined whether kinetic physics can play a more significant role in other types of events, including but not limited to substorms.

1. Introduction

A geomagnetic storm is a major disturbance of Earth's magnetosphere that occurs when a significant amount of energy is deposited into the geospace. The most widely used and successful simulation tools to study the geomagnetic storms are based on the magnetohydrodynamic (MHD) description, which is computationally feasible to solve. The first global MHD models were developed in the 1980s (Brecht et al., 1981, 1982; LeBoeuf et al., 1981; Wu et al., 1981). Later on, models with more advanced numerical algorithms have been developed, such as the Lyon-Fedder-Mobarry (LFM) (Lyon et al., 1986; Lyon et al., 2004), the OpenGGCM (Raeder et al., 1995, 1996), and the GUMICS (Grand Unified Magnetosphere Ionosphere Coupling Simulation) model (Janhunen, 1996).

In this paper, we use the University of Michigan's Space Weather Modeling Framework (SWMF (Tóth et al., 2012)), which also includes an MHD model, the Block Adaptive-Tree Solar-wind Roe-type Upwind Scheme (BATS-R-US) (Powell et al., 1999), as its Global Magnetosphere (GM) component. The SWMF has been applied to many storm event simulations (Glocer et al., 2009; Haiducek et al., 2017; Tóth et al., 2007) and has also been selected as the physics-based model at the Space Weather Prediction Center based on a thorough model comparison (Pulkkinen et al., 2013).

Magnetic reconnection plays a key role in the magnetosphere both at the dayside and in the tail. Despite all the successful applications MHD models have achieved, magnetic reconnection in the global MHD models relies on either Hall resistivity, or ad hoc anomalous resistivity, or simply numerical diffusion. The numerical diffusion plays an important role in both ideal and Hall MHD models because it is required to break the field lines. As we show in Appendix A, the reconnection rate remains finite when the grid resolution becomes finer. The Hall resistivity, although does not break the field lines that are frozen into the electron fluid, changes the structure of the reconnection region, which can lead to a faster reconnection rate than ideal MHD (Birn et al., 2001). A current dependent anomalous resistivity has also been applied in MHD simulations (Raeder et al., 2001). However, none of these approximations truly describe the physical processes responsible for collisionless reconnection. It is very important to properly represent kinetic reconnection physics in a global simulation and check if it plays

an important role in contributing to the larger scale processes that eventually produce geomagnetic disturbances and space weather effects. Furthermore, the MHD approximation assumes that the distribution functions of the ions and electrons are Maxwellian. Numerous observations suggest that this condition is violated especially near the magnetic reconnection sites (Burch et al., 2016; Chen et al., 2016; Hwang et al., 2019; Lotekar et al., 2020).

The MHD with embedded particle-in-cell (MHD-EPIC) model (Daldorff et al., 2014) enables kinetic physics to be introduced into a global MHD model. The MHD-EPIC model has been successfully used to study the interaction between the Jovian wind and Ganymede's magnetosphere (Tóth et al., 2016; Zhou et al., 2019, 2020), flux transfer events (FTEs) at Earth's dayside magnetopause (Chen et al., 2017), Mars' magnetotail dynamics (Ma et al., 2018), and the dawn-dusk asymmetries discovered at Mercury's magnetotail (Chen et al., 2019). However, the iPIC3D (Markidis et al., 2010) code, which is the PIC model used in the MHD-EPIC simulations, can only run on a fixed Cartesian grid. The magnetotail (and the associated current sheet that contains the reconnection sites) typically exhibits a flapping motion (Tsumoto & Teruki, 1976; Volwerk et al., 2013) during geomagnetic storms. Covering the whole domain of interest where reconnection can occur in the magnetotail would require a very large PIC grid and would result in a massive computational cost. This may be feasible for a short simulation time (up to an hour or so) but geomagnetic storms that usually happen last for days, and the computational cost would become prohibitive.

To tackle this problem, we have developed the MHD with adaptively embedded PIC (MHD-AEPIC) algorithm that allows a smaller PIC region than MHD-EPIC, which saves computational resources. Shou et al. (2021) introduce this idea and verifies that covering part of the simulation domain with a dynamically moving PIC box gives the same solution as using a larger fixed PIC domain, while running significantly faster. This justifies our effort to use an adaptive PIC region in the simulation. In this paper, we further improve this method and make it more flexible: (a) The size and shape of the active PIC regions can be adapted during the runtime; (b) the adaptation of the active PIC region is fully automatic. To realize the first feature, instead of iPIC3D, we use the flexible exascale kinetic simulator (FLEKS) (Chen et al., 2021) as the PIC model. FLEKS inherits all numerical algorithms from MHD-EPIC and also accommodates an adaptive PIC grid that allows PIC cells to be turned on and off during the simulation. In addition, FLEKS employs a particle splitting and merging scheme to improve the simulation efficiency and accuracy. FLEKS is described in more detail in Section 2.2.

We have developed a reliable and efficient algorithm to identify potential reconnection sites in the magnetotail using three local criteria. The criteria are easy to compute and provide the information to the FLEKS code to adapt its grid to cover the reconnection sites. This newly developed MHD-AEPIC model is applied to simulate a magnetic storm. The SWMF simulation involves BATSRUS, FLEKS, the ionosphere electrodynamic model, Ridley Ionosphere Model (RIM; Ridley et al., 2004), and the Inner Magnetosphere (IM) model, Rice Convection Model (RCM; Toffoletto et al., 2003; Wolf et al., 1982). This is the first simulation of a real event with kinetic reconnection physics in the magnetotail scaling from the global scales of the magnetosphere to the electron scales near the reconnection sites.

In this paper, we employ the new model to simulate the magnetic storm of 2011-08-05. We cover the tail reconnection sites with the adaptive PIC model. We also perform ideal MHD and Hall MHD simulations for comparison. All simulations are fully coupled with the IM and ionospheric electrodynamic models within the Space Weather Modeling Framework. We focus on the impact of using ideal MHD, Hall MHD, and MHD-AEPIC physics on the dynamical processes in the magnetotail. To make the comparison straightforward, we use the ideal MHD model at the dayside in all three simulations.

The computational methods are described in Section 2, the demonstration of the adaptation feature and comparisons between models and observations are shown in Section 3, and we summarize in Section 4.

2. Methods

2.1. Global Magnetosphere Model: BATS-R-US

The Block-Adaptive Tree Solar-wind Roe-type Upwind Scheme (BATS-R-US) is used as the GM model in our simulation. In the Hall MHD and MHD-AEPIC simulations in this paper, the Hall MHD equations (Tóth et al., 2008) are solved. The Hall term is handled with a semi-implicit scheme. The spatial discretization uses a second order accurate TVD scheme with the Artificial Wind Riemann solver (Sokolov et al., 1999) and the Koren

limiter (Koren, 1993) with $\beta = 1.2$. The hyperbolic cleaning (Dedner et al., 2003) and eight-wave scheme (Powell et al., 1999) are used to keep the magnetic field approximately divergence-free.

The Hall MHD equations with a separate electron pressure equation are

$$\frac{\partial \rho}{\partial t} = -\nabla \cdot (\rho \mathbf{u}) \quad (1)$$

$$\frac{\partial(\rho \mathbf{u})}{\partial t} = -\nabla \cdot \left[\rho \mathbf{u} \mathbf{u} + (p + p_e) \bar{I} + \frac{B^2}{2\mu_0} \bar{I} - \frac{\mathbf{B}\mathbf{B}}{\mu_0} \right] \quad (2)$$

$$\frac{\partial e}{\partial t} = -\nabla \cdot \left[(\epsilon + p) \mathbf{u} + p_e \mathbf{u}_e + \mathbf{u}_e \cdot \left(\frac{B^2}{\mu_0} \bar{I} - \frac{\mathbf{B}\mathbf{B}}{\mu_0} \right) \right] + p_e \nabla \cdot \mathbf{u}_e \quad (3)$$

$$\frac{\partial \mathbf{B}}{\partial t} = -\nabla \times \left[-\mathbf{u}_e \times \mathbf{B} - \frac{\nabla p_e}{ne} \right] \quad (4)$$

$$\frac{\partial p_e}{\partial t} = -\nabla \cdot (p_e \mathbf{u}_e) - (\gamma - 1) p_e \nabla \cdot \mathbf{u}_e \quad (5)$$

where \bar{I} is the identity matrix, ρ is the mass density, \mathbf{u} is the plasma bulk velocity, \mathbf{B} is the magnetic field, p_e is the electron pressure, p is the ion pressure, and $\mathbf{j} = \nabla \times \mathbf{B}/\mu_0$ is the current density. The Hall velocity and electron bulk velocity are defined as

$$\mathbf{v}_H = -\frac{\mathbf{j}}{ne} = -\frac{M_i}{e} \frac{\mathbf{j}}{\rho} \quad (6)$$

$$\mathbf{u}_e = \mathbf{u} + \mathbf{v}_H \quad (7)$$

where $n = \rho/M_i$ is the number density, M_i is the ion mass, and e is the elementary charge. The total energy density is defined as

$$e = \epsilon + \frac{B^2}{2\mu_0} = \frac{1}{2} \rho \mathbf{u}^2 + \frac{p}{\gamma - 1} + \frac{B^2}{2\mu_0} \quad (8)$$

where $\epsilon = \rho \mathbf{u}^2/2 + p/(\gamma - 1)$ is the hydrodynamic energy density of the ions and $\gamma = 5/3$ is the adiabatic index. The thermal energy density of the electrons is $\epsilon_e = p_e/(\gamma - 1)$. We note that the $e + \epsilon_e$ is conserved both analytically and numerically as the nonconservative source terms $\pm p_e \nabla \cdot \mathbf{u}$ in Equations 3 and 5 cancel out. Apart from $(\rho, \mathbf{u}, \mathbf{B}, p, p_e)$, other variables are derived quantities.

The continuity Equation 1, momentum Equation 2, energy Equation 3, and electron pressure Equation 5 are solved with an explicit time stepping scheme. In the induction Equation 4, the convection term $\mathbf{u} \times \mathbf{B}$ and pressure gradient term $\nabla p_e/ne$ are solved using an explicit scheme, while the Hall term $\mathbf{v}_H \times \mathbf{B}$ is advanced with an implicit scheme. The Hall MHD equations introduce the whistler mode wave, which has a characteristic wave speed inversely proportional to the wavelength. The shortest wavelength that exists in a numerical simulation is proportional to the cell size Δx , so the fastest whistler wave speed in a simulation is proportional to $1/\Delta x$. The time step in a fully explicit scheme is limited by the Courant-Friedrichs-Lewy (CFL) condition: $\Delta t < \Delta x/c_{\max}$, where c_{\max} is the fastest wave speed, which leads to a time step proportional to $1/(\Delta x)^2$. We use a semi-implicit scheme (Tóth et al., 2012) to handle the stiff Hall term in the induction equation so that the time step of the explicit part is only limited by the fast magnetosonic wave speed instead of the whistler speed.

A three-dimensional block-adaptive Cartesian grid is used to cover the entire computational domain $-224 R_E < x < 32 R_E$, $-128 R_E < y$, $z < 128 R_E$ in GSM coordinates. The Hall effect is restricted to $x \in [-100 R_E, 20 R_E]$, $|y| < 30 R_E$ and $|z| < 20 R_E$ box regions excluding a sphere of radius $3 R_E$ centered at Earth to speed up the simulation. Outside this region, the Hall effect is neglected by setting $\mathbf{v}_H = 0$. In the magnetosphere, the smallest ion inertial length $d_i = c/\omega_{pi}$ is about $1/20 R_E$ in the tail lobe region, which is already extremely difficult for a 3-D global MHD model to resolve, let alone the PIC code. Tóth et al. (2017) introduced a scaling approach that scales up the kinetic length by artificially increasing ion mass per charge by a scaling factor. The scaling does not change the fluid variables, such as density, pressure, velocity, IMF, and dipole field, and the global structure of

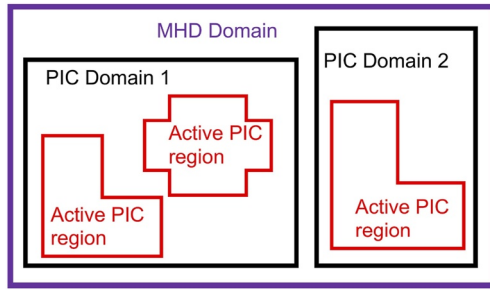


Figure 1. The schematic plot of the flexible exascale kinetic simulator adaptive grid. The red line boundary shows the flexibility of turning on and off the particle-in-cell patches during the simulation.

the magnetosphere will not change significantly as long as the scaled-up ion inertial length is much smaller than the global scales. In this paper, we use a factor of 16, which satisfies this condition. On the other hand, with the ion inertial length scaled up by 16 times, we do not need an extremely fine grid to resolve it. We set the grid cell size in the magnetotail to $\Delta x = 1/4 R_E$, which is about 4 times smaller than the scaled-up ion inertial length. About 14 million cells are used in total. For MHD model simulations, we also apply a $1/8 R_E$ grid resolution in the tail: $x \in [-60 R_E, -10 R_E]$ and $|y|, |z| < 10 R_E$. This increases the total number of cells to about 23 million, which is still feasible to do (but would be too expensive for the MHD-AEPIC model). Comparing the simulation results with $1/4 R_E$ and $1/8 R_E$ resolutions in the tail allows us to look into the role of numerical resistivity.

At the inner boundary $r = 2.5 R_E$, the density is calculated using the empirical formula $\rho_{\text{inner}} = (28 + 0.1\text{CPCP}) \text{ amu/cm}^3$, where CPCP is the average of the northern and southern cross polar cap potentials (CPCP) measured in keV. This boundary condition has been used successfully in previous geomagnetic storm simulations (Pulkkinen et al., 2013). The pressure and the magnetic field \mathbf{B}_1 (excluding dipole field) have zero gradient at the inner boundary, while the radial velocity is set to zero and the tangential velocity is calculated from the corotation and the $\mathbf{E} \times \mathbf{B}$ drift, where the electric field \mathbf{E} is provided by the RIM (Ridley et al., 2004).

2.2. Particle-In-Cell Model: FLEKS

The FLEKS (Flexible Exascale Kinetic Simulator) (Chen et al., 2021) is used as the PIC model (PC component in the SWMF) to resolve kinetic physics. FLEKS uses the same two-way coupling method as MHD-EPIC (Daldorff et al., 2014) and the Gauss's law satisfying energy-conserving semi-implicit method (GL-ECSIM) (Chen & Tóth, 2019) for the PIC solver. To enable the adaptation in MHD-AEPIC, FLEKS introduces an adaptive grid that allows changing the simulation region dynamically. Figure 1 shows a schematic plot of the adaptive grid. We choose $\Delta x = 1/4 R_E$ to be the PIC grid resolution so that the scaled $d_i/\Delta x \sim 4$. The ion inertial length inside the magnetosphere is described in Subsection 2.1. The ion-electron mass ratio is set to 100 in this simulation so that the electron skin depth $d_e = 0.1 d_i$. Li et al. (2019) perform 2-D PIC simulations using different ion-electron mass ratios and conclude that features such as reconnection rate and magnetic energy conversion are similar in simulations using different ion-electron mass ratios. Although the grid is not refined to resolve the electron scale, in the PIC model, the electron particles can resolve sub-grid scale physics under the influence of the electromagnetic field that is resolved on the ion scale. Chen and Tóth (2019) show that the semi-implicit PIC model can reproduce the most important ion scale features of magnetic reconnection with $d_i/\Delta x \sim 4$. The selected resolution balances between the computational cost and the requirement of resolving kinetic scales.

FLEKS provides a particle merging and splitting scheme to maintain the number of particles per cell within bounds. Merging particles in a cell with high number of particles can improve load-balancing and speed up simulation, while splitting particles in a cell with few particles can reduce noise and improve accuracy for the PIC simulation. This feature is very useful keeping the number of particles per cell about uniform during a long geomagnetic storm simulation.

2.3. Selection Criteria of PIC Regions

As described in the previous section, FLEKS allows patches to be turned on and off during the simulation. To make the active PIC patches only cover the regions of interest, where magnetic reconnection is happening or will be triggered soon, the MHD model should locate these regions and pass this information to FLEKS. Finding the locations of magnetic reconnection sites can be done in various ways, including tracing field lines (Glocer et al., 2016). For sake of efficiency and generality, here we use local criteria based on the local MHD solution only.

Magnetic reconnection usually happens in current sheets where the current density j is strong and the magnetic field B is weak. In particular, the field B_{\perp} that is perpendicular to the current \mathbf{j} should be close to zero, while the

guide field parallel to the current can be nonzero. We define the following nondimensional relation as our first criterion:

$$\frac{J \Delta x}{B_{\perp} + \varepsilon} = \frac{J^2 \Delta x}{|\mathbf{J} \times \mathbf{B}| + J \varepsilon} > c_1 \quad (9)$$

where $\mathbf{J} = \mu_0 \mathbf{j} = \nabla \times \mathbf{B}$ and ε is a small dimensional constant in units of the magnetic field, introduced to avoid dividing by zero. We use $\varepsilon = 1$ nT in our simulations presented here, which is much smaller than the typical magnetic field intensity in the tail current sheet. Δx is the local cell size that is used in calculating the curl of the magnetic field so that $J \Delta x$ is the jump of the transverse magnetic field between neighboring grid cells. We set $c_1 = 0.8$ in this work to select the cells that are close to the reconnection sites.

While criterion (Equation 9) works quite well in general, we sometimes find that it selects the axis of flux ropes, or O-lines, in addition to X-lines, especially if ε is very small. Reconnection does not occur at O-lines, so we developed a second criterion that distinguishes X- and O-lines based on the divergence of the magnetic field curvature vector:

$$[\nabla \cdot (\mathbf{b} \cdot \nabla \mathbf{b})](\Delta x)^2 > c_2 \quad (10)$$

where $\mathbf{b} = \mathbf{B}/|\mathbf{B}|$ is a unit vector along the magnetic field. We use $c_2 = -0.1$ to identify X-lines where the curvature vectors point away from the X-line, so their divergence is positive.

The above two criteria are identifying potential magnetic reconnection sites through local plasma properties in a general scenario. However, current sheets in the solar wind can also satisfy those two criteria. To make the selection more selective, we need to introduce a third criterion to exclude the volume outside the magnetosphere. Observations show that specific entropy is two orders of magnitude larger in the magnetosphere than in the magnetosheath (Ma & Otto, 2014) and our simulations properly reproduce these properties. Here, we use the specific entropy as the third criterion:

$$\frac{p}{\rho^\gamma} > c_3 \quad (11)$$

where p is the plasma thermal pressure, ρ is the plasma density, and $\gamma = 5/3$ is the ratio of the specific heats (Birn et al., 2006, 2009). Different from the c_1 and c_2 introduced above, this criterion is dimensional and we use the threshold value $c_3 = 0.02$ nPa/cm^{-3 γ} .

The three criteria combined can identify X-lines in the magnetotail well. To make the active PIC region large enough around the X-lines, we flag all patches where all three criteria are met and then activate all patches within a distance L_x , L_y , and L_z from these flagged patches in the x , y , and z directions, respectively. The extension in each direction enables the PIC model to cover a buffer area outside the reconnection sites. This buffer ensures that the velocity distribution of ions and electrons at the boundary of the PIC region can be well approximated with a drifting Maxwellian distribution, which results in a consistent coupling between the MHD models. We use $L_x = 4 R_E$ and $L_y = L_z = 2 R_E$ in this work.

Each MPI process of BATS-R-US calculates the above criteria on their respective sub-domains overlapping with the PIC grid and activates the patches of the PIC grid where all three criteria are satisfied. Then the processors collect the information: a PIC patch is activated if any of the BATS-R-US processes activated it. Since the status of all PIC patches (on/off) is stored in each MPI processor of BATS-R-US, using the default logical array would consume a lot of memory. To reduce the memory use, the status is stored by a single bit, which is 32 times smaller than the size of the default logical variable in Fortran. The information is conveniently collected with the bitwise “or” operator, `MPI_BOR`, used in the `MPI_ALLREDUCE` call.

2.4. Ionospheric Electrodynamics Model: RIM

The Ionospheric Electrodynamics (IE) is simulated by the RIM (Ridley et al., 2004) that solves a Poisson-type equation for the electric potential on a 2-D spherical grid. In this work, the grid resolution is set to 2° in both longitude and latitude directions. The lower latitude boundary is at 10° where the electric potential is set to zero.

The BATS-R-US and RIM models are two-way coupled every 5 s. To calculate the Poisson-type equation, RIM obtains the field-aligned currents (FAC) calculated at $3 R_E$ from the BATS-R-US model and maps them down to its grid. The F10.7 flux is also an input parameter of RIM that is used together with the FAC to calculate the particle precipitation and conductances based on an empirical model. The electric field calculated by the RIM is mapped back to the inner boundary of BATS-R-US to obtain the $\mathbf{E} \times \mathbf{B}/B^2$ velocity for its inner boundary condition. The CPCM, the difference of the maximum and minimum potentials in the two hemispheres) are also sent to BATS-R-US to set the density at the inner boundary.

2.5. Inner Magnetosphere Model: RCM

The IM is modeled by the RCM (Toffoletto et al., 2003; Wolf et al., 1982). The standard RCM settings are used, including an exponential decay term with a 10-hr e-folding rate. The decay term makes the Dst index recover better after strong storms. As a component of the SWMF geospace model, RCM is used in all simulations presented in this paper.

The RCM model is one-way coupled with RIM and two-way coupled with BATS-R-US every 10 s. RIM sends the electric potential to RCM, where it is used to advect the field lines with the $\mathbf{E} \times \mathbf{B}/B^2$ drift. In the two-way coupling between BATS-R-US and RCM, BATS-R-US identifies the closed field line regions and calculates field volume integrals of pressure and density (De Zeeuw et al., 2004). The integrated pressure and density are applied to RCM as the outer boundary condition with the assumption of 90% H^+ and 10% O^+ number density composition. From RCM to BATS-R-US, the GM grid cell centers are traced to the RCM boundary along the magnetic field lines (De Zeeuw et al., 2004) and the BATS-R-US pressure and density are pushed toward the RCM values with a 20 s relaxation time.

3. 3D Global Simulation With Kinetic Physics in the Magnetotail

3.1. Simulation Setup

We apply the MHD-AEPIC method to the geomagnetic storm event of 6 August 2011, with an observed minimum Dst -126 nT. Previous modeling works show frequent flapping motion of the magnetotail current sheet during the storm (Tsutomu & Teruki, 1976; Volwerk et al., 2013), so the adaptive embedding feature is perfect for only covering the current sheet during the simulation. We start our simulation at 2011-08-05 15:00:00 and end it at 2011-08-06 07:00:00. This time range covers the main phase and the early recovering phase of the storm when the largest geomagnetic impact happens. The solar wind inputs are shown in Figure 2. First, the BATS-R-US and RIM models are run to reach a quasi-steady state after 50k iteration steps using local time stepping. Figure 3 shows the plasma density along with the different refinement level boundaries of the AMR grid in the meridional plane for the steady state-solution. Then, the SWMF is switched to a time-accurate mode with the FLEKS and RCM models turned on. Chen et al. (2017) and Zhou et al. (2020) study the dayside reconnection at Earth and Ganymede by putting PIC regions at the magnetopause. They also compare the results with Hall MHD and conclude that the two models generate similar global features, such as flux rope formation and reconnection rate. In this paper, we only put PIC regions in the magnetotail in order to control variants. The dayside reconnection is modeled by the ideal MHD. The computational domain of FLEKS is determined by the selection criteria introduced above. For the sake of comparison, we also conduct two other simulations without FLEKS: one with the Hall MHD model and the other with the ideal MHD model.

3.2. PIC Region Adaptation

In this subsection, we highlight the utility and efficiency of the adaptive embedding scheme. Figure 4 illustrates how the PIC region is changing over the simulation. Panels (a)–(f) are snapshots from six different times. The color contours show the j_y component of the current density on the meridional plane to show the magnetospheric current system. Boundaries of the active PIC region are shown by the gray isosurface. Snapshots 4 (a) and (b) are taken before the sudden commencement of the storm. At this time, the IMF B_z is pointing northward and the solar wind speed is about 400 km/s. From the isosurface plot, the PIC region is covering the tail current sheet tilting southward. In Figure 4b, the tail current sheet is kinked and the PIC region adjusts its shape to accommodate the tail current sheet. Snapshots 4 (c)–(f) are taken after the sudden commencement of the storm. Here, we

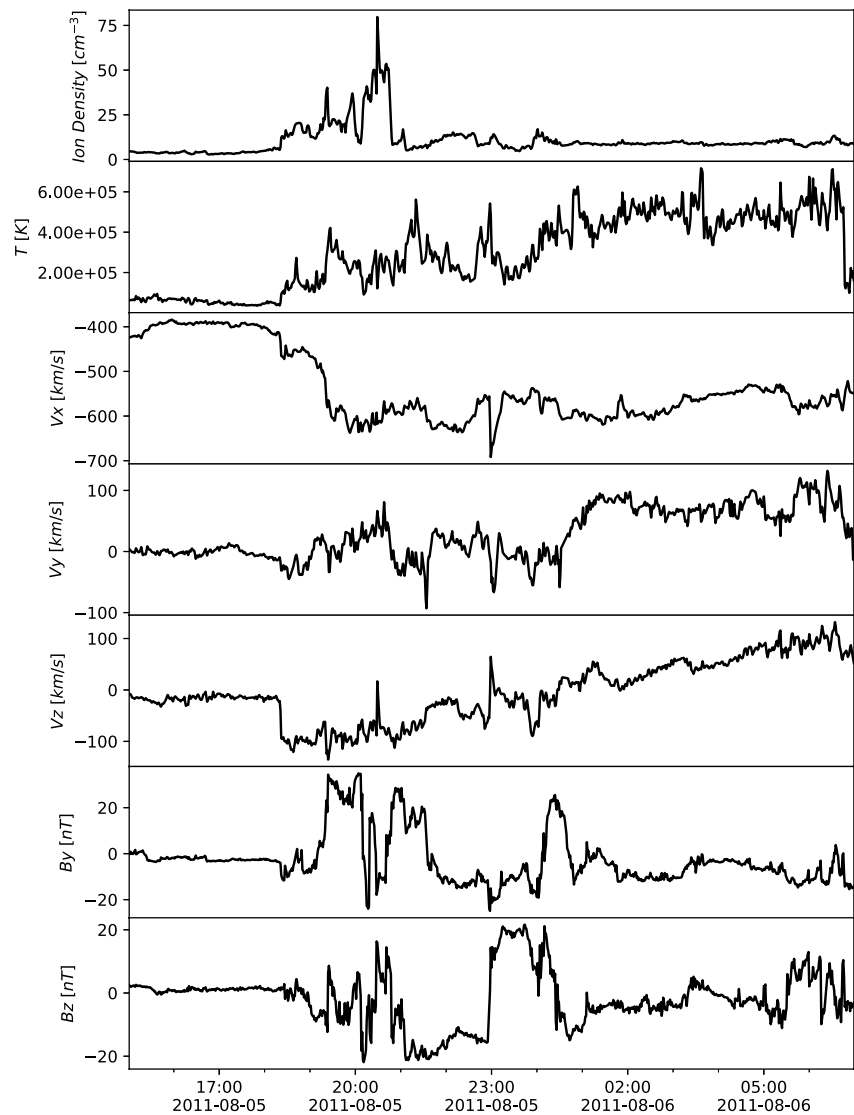


Figure 2. The solar wind bulk plasma and interplanetary magnetic field input in Geocentric Solar Magnetospheric coordinates (from the top panel to the bottom: plasma density, plasma temperature, x , y , and z components of the plasma flow velocity, and y and z components of the magnetic field) for the simulation in this paper. The x -component of the magnetic field is set to be zero. The solar wind data are obtained from the ACE spacecraft observation and propagated to the bow shock position (Pulkkinen et al., 2013).

observe a much compressed magnetosphere as well as an enhanced current density. In the last two snapshots, the tail current sheet is tilting northward and it is well covered by the PIC region. From the snapshots, we can conclude that the PIC region selection criteria work well in identifying the tail current sheet, which can make the PIC region accommodate with the flapping motion of the magnetotail. The translucent red line in Figure 4g shows the volume of the active PIC region recorded every second from the simulation, while the solid red line is the volume smoothed over every minute. The Dst index is also presented in the background for reference. The volume of the PIC region increases after the sudden commencement and starts dropping in the recovering phase. This reflects that the tail current system intensity is related to the solar wind condition. Notice that the volume is less than $16,000 R_E^3$ for the entire storm simulation, which is only about 11.2% of the large PIC box extending from $-100 R_E$ to $-10 R_E$ in the x direction and $-20 R_E$ to $20 R_E$ in the y and z directions. This confirms that the MHD-AEPIC method saves a substantial amount of computational resources.

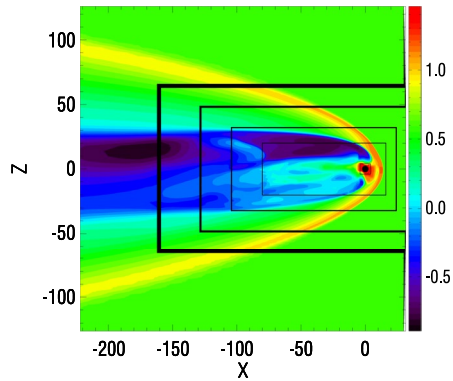


Figure 3. The meridional plane of the simulation domain. The color contour shows the plasma density of the steady state on a logarithmic scale. The black lines show the boundaries between different refinement levels. The refinement ratio between two adjacent levels is two. The grid resolution near Earth is $1/8 R_E$ and it is $1/4 R_E$ on the dayside and the magnetotail out to $x > -80 R_E$.

3.3. Global Scale: Geomagnetic Indexes and Ionospheric Quantities

To evaluate the models' performance at the global scale, we use the SYM-H and SME as evaluation metrics. The SYM-H index approximates the symmetric portion of the northward component of the magnetic field near the equator based on measurements at six ground magnetometer stations. This index characterizes the strength of the ring current (Ganushkina et al., 2017) and it is an indicator of storm activity. The SYM-H data with a 1-min cadence are downloaded from the NASA OMNIWeb Data Service. The SuperMAG electrojet (SME) index is an indicator of substorms and auroral power (Newell & Gjerloev, 2011). SME utilizes more than 100 ground magnetometer stations at geomagnetic latitudes between $+40^\circ$ and $+80^\circ$, which resolves the large and extreme events more effectively than the traditional Auroral Electrojets (AE) index (Bergin et al., 2020; Davis & Sugiura, 1966).

In our model, the simulated SYM-H is calculated by evaluating the Biot-Savart integral at the center of Earth from all currents in the simulation domain. Calculating SME is more complicated: the magnetic field disturbances are calculated at the positions of the 100+ ground magnetometer stations and the simulated SME is obtained following the SuperMAG procedure. From

Figure 5, the MHD-AEPIC produces geomagnetic indexes close to the other two MHD models. The SYM-H plot shows that the initial, main, and recovery phases of the storm event are reproduced by all three models reasonably well. However, the models cannot reproduce the lowest SYM-H values that correspond to the strongest observed geomagnetic perturbations. This feature can also be observed in the SME plots: all three models produce increased auroral electrojets; however, the second and third enhancements are weaker than the observed values. For MHD model simulations, the root mean square errors (RMSE) of SYM-H and SME are not changing much from the $1/4 R_E$ to $1/8 R_E$ grid resolutions as shown in Figure 5. This means that the numerical diffusion is not the major reason for the similarity of global indexes generated from the three models, which demonstrates that the numerical diffusion effect is converged to some extent on the $1/4 R_E$ grid resolution in the tail. Fine grid resolution toward $0.1 R_E$ is also applied in simulations using the LFM model (Merkin et al., 2019; Wiltberger et al., 2015) and the authors demonstrate that the reconnection will not be significantly suppressed if the grid resolution is further increased.

Apart from the global indexes such as SYM-H and SME, it is also important to compare the amount of energy that the solar wind and interplanetary magnetic field (IMF) transfer to Earth's magnetosphere-ionosphere system through direct driving. The CPCP is an indicator of this energy transfer process (Troshichev et al., 1988, 1996). The CPCP is not directly measured but can be derived from observations using the Assimilative Mapping of Ionospheric Electrodynamics (AMIE) (Richmond & Kamide, 1988) technique or from the Defense Meteorological Satellite Program (DMSP) measurements (Hairston et al., 1998). Another approach based on the Super Dual Auroral Radar Network (SuperDARN) observations (Ruohoniemi & Greenwald, 1998) usually underestimates the CPCP significantly. We opt to use the readily available Polar Cap Index (PCI) from the OMNIWeb website and convert it into CPCP using the empirical relationship derived by Ridley and Kihn (2004):

$$\text{CPCP}_{\text{North}} = 29.28 - 3.31\sin(T + 1.49) + 17.81\text{PCLN} \quad (12)$$

where T is the month of the year normalized to 2π . The storm event in this paper is in August, so $T = (8 - 1) * 2\pi / 12$. Gao (2012) showed that this formula provides good agreement with AMIE and DMSP based approaches. For the southern hemisphere, since there is no published empirical relationship between southern CPCP and PCI, we change the sign in front of the $\sin(T + 1.49)$ term (expressing the seasonal dependence) in the formula:

$$\text{CPCP}_{\text{South}} = 29.28 + 3.31\sin(T + 1.49) + 17.81\text{PCLN} \quad (13)$$

The simulated CPCP is defined as the difference between the maximum and the minimum of the electric potential obtained from the RIM model for both hemispheres.

Figure 6a shows the northern and southern CPCP from the three models together with the CPCP derived from the PCI. In general, the results from the three models are very close to each other and have good agreements with the

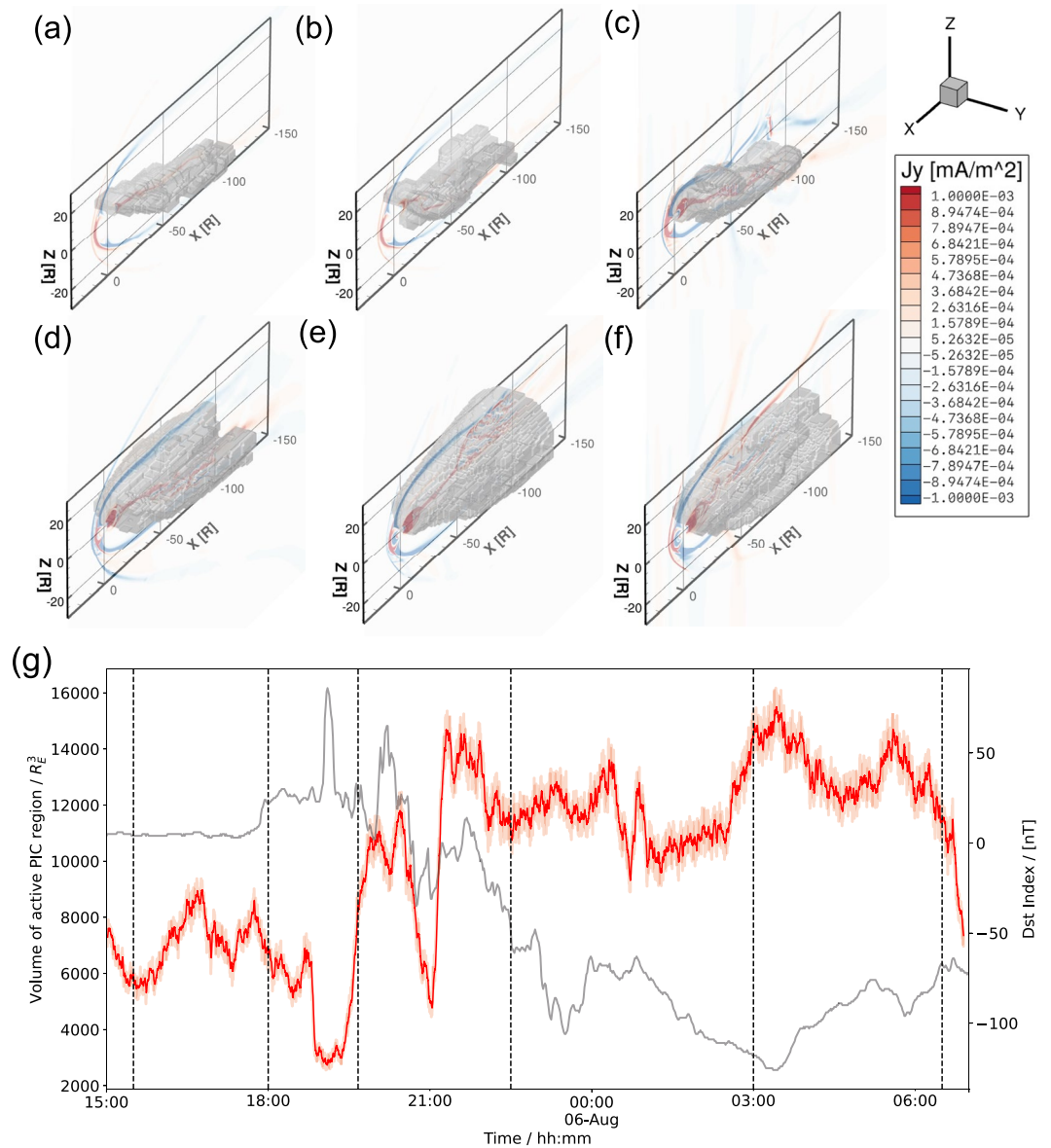


Figure 4. (a–f) Demonstration of particle-in-cell (PIC) region adaptation during the simulation. The contour plot of j_y in the meridional plane is showing the general condition of the magnetospheric current system. The active PIC region boundary is shown by a gray isosurface. (g) Time evolution of the active PIC region volume. The translucent red line is the output every second and the solid red is the output smoothed every minute. The Dst index is plotted as a gray line for reference. The six vertical dashed lines correspond to the times of the snapshots (a)–(f), respectively.

PCI derived CPCP for both hemispheres. Notice that the PCI is derived from a single station for each hemisphere while the model calculates CPCP using the entire electric potential. The differences between the model output and CPCP could be because the PCI is not measuring the ionospheric dynamics for the entire polar region. We observe that the three models generate the most different CPCP results during the main phase of the storm event at around $t = 2011-08-05 22:00:00$. Figure 6b shows the polar cap potential and radial component of the FAC for both hemispheres. The structure of the electric potentials as well as the FAC are very similar among the three models.

The geomagnetic indexes and ionospheric quantities demonstrate that introducing kinetic physics in the magnetotail does not change the global configuration of the simulated magnetosphere and ionosphere significantly

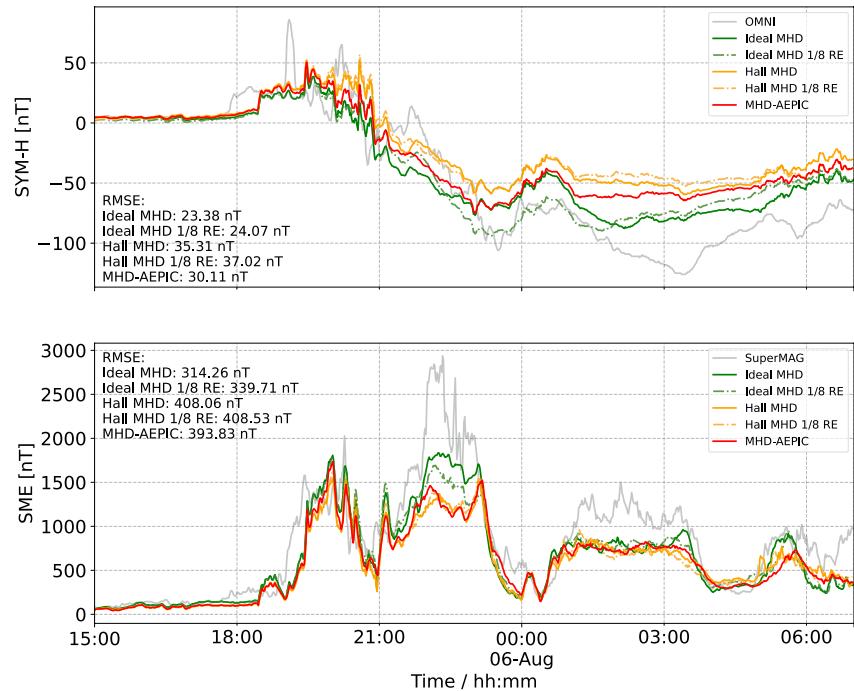


Figure 5. 6 August 2011 storm. Colored lines show the SYM-H and SuperMAG electrojet indexes from five simulations from three different models and the gray line corresponds to the observed indexes. The root mean squared error between the simulated indexes and observations are also presented.

relative to the ideal and Hall MHD simulations. It is to be seen if this trend persists for other storms, especially extreme events.

3.4. Mesoscale: Magnetotail Dynamics

During the storm event, the Geotail spacecraft was in the magnetotail at $x \approx -29 R_E$ crossing the equatorial plane and approaching to the meridional plane. Figure 7 shows the magnetic field and ion moments observed by Geotail and compares them with the ideal-MHD, Hall-MHD, and MHD-AEPIC simulations. The MHD-AEPIC model shows a reasonable agreement with the Geotail number density observation before $t = 2011-08-06 00:00$, including the current sheet crossing event between $t = 2011-08-05 22:00$ and $t = 2011-08-05 23:00$, while the Hall-MHD model overestimates the ion number density substantially. However, all three models generate much higher number densities than observed after $t = 2011-08-06 00:00$. None of the three models show perfect agreement with the magnetic field observations. The B_x component gives us information about which side of the current sheet the satellite is. The comparison plot shows that the virtual satellites in the simulations are all on the opposite side of the current sheet than Geotail before $t = 2011-08-05 22:00$. Between $t = 2011-08-05 23:00$ and $t = 2011-08-06 01:00$, Geotail is crossing the current sheet from the north side to the south side, and this is captured by all three models. However, the next current sheet crossing at around $t = 2011-08-06 01:30$ is not captured by MHD-AEPIC and ideal-MHD. The Hall-MHD simulations produce a similar structure but with a 30-min time shift. The B_y and B_z components give information about the flux rope structures. All three models provide good agreement with the observation in terms of the overall field magnitude, while it is difficult to tell which one is better in capturing fine details. Geotail observed a B_z reversal along with a relatively strong core B_y at around $t = 2011-08-06 05:00$, which indicates a flux rope. A similar structure is produced by MHD-AEPIC with a 30-min delay, while there is no similar signal from the ideal-MHD and Hall-MHD simulations. Geotail observed high ion speed of around 1,000 km/s at $t = 2011-08-06 02:00$ and $t = 2011-08-06 03:00$. The MHD-AEPIC model only generates around 500 km/s ion speeds. Although the ideal-MHD and Hall-MHD models can produce maximum ion speeds of around 1,000 km/s, they also generate large scale oscillations that are not present in the observations. Overall, introducing kinetic physics in the magnetotail did not improve plasma and magnetic

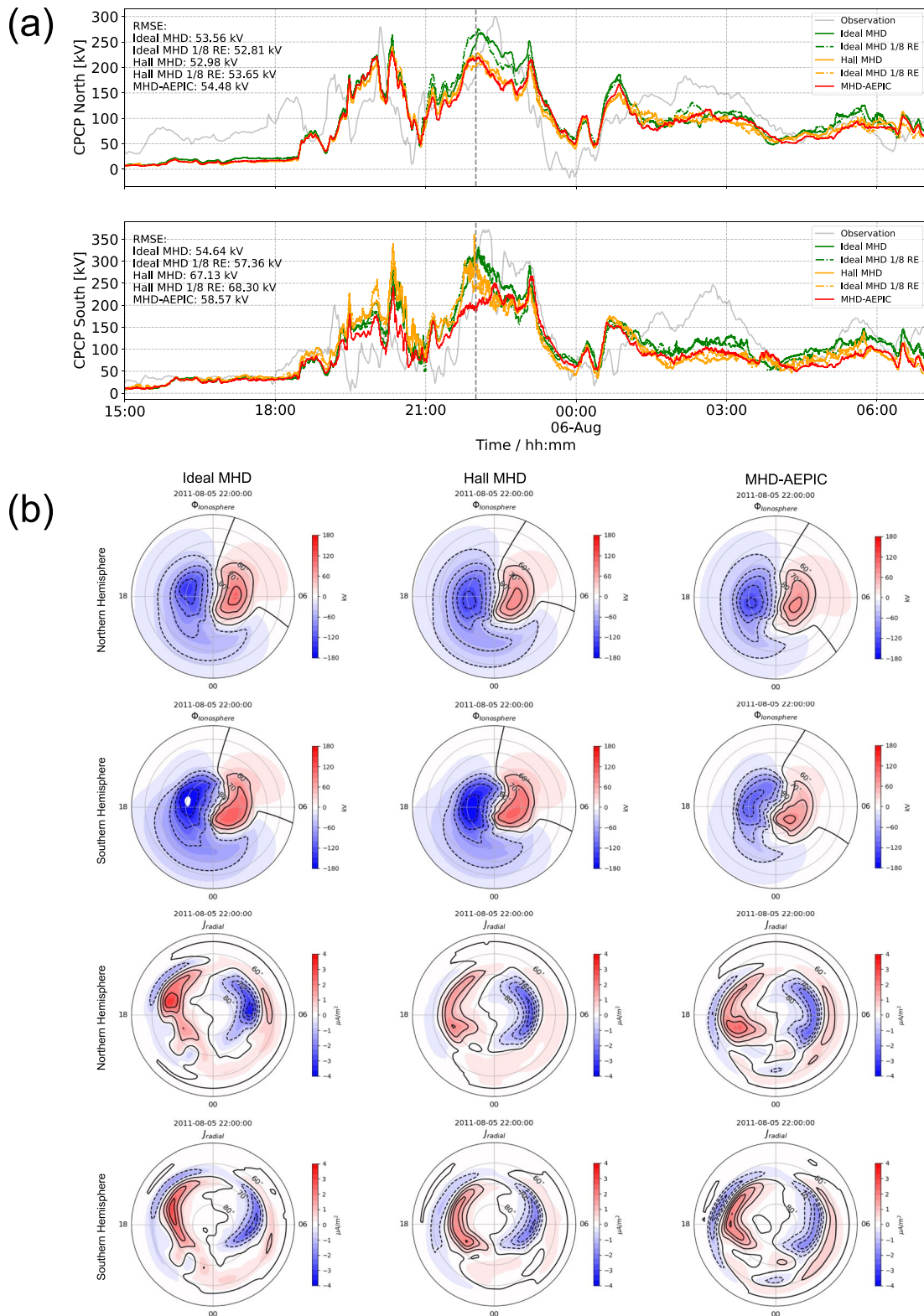


Figure 6. (a) The northern and southern cross polar cap potentials (CPCP) of the 6 August 2011 storm. Colored lines are model outputs, the gray line is the CPCP estimated (Ridley & Kihn, 2004) from the observed Polar Cap Index. The root mean squared error between the simulated indexes and observations are also presented. (b) The northern and southern electric potentials and the radial current from the three models at 2011-08-05 22:00:00 (marked with a vertical dashed line in panel (a)).

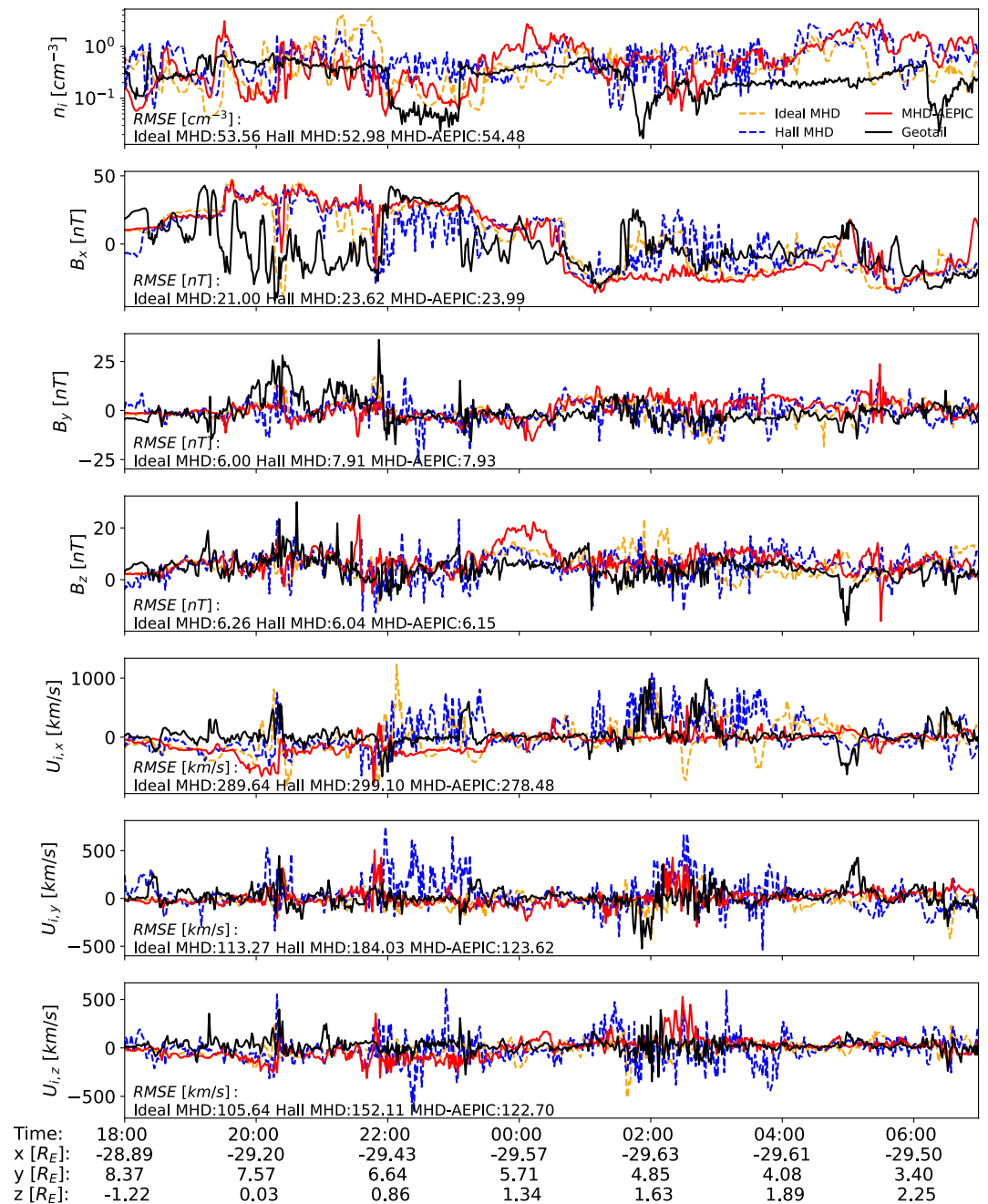


Figure 7. The ion density, magnetic field components, and the ion velocity components observed by the Geotail spacecraft and the SWMF ideal magnetohydrodynamic (MHD), Hall MHD, and MHD with adaptively embedded particle-in-cell (MHD-AEPIC) simulations. The root mean squared error between the model outputs and observations are presented. The time interval shown starts from $t = 2011-08-05$ 18:00:00 right before the sudden commencement to $t = 2011-08-06$ 00:07:00 at the beginning of the recovery phase of the geomagnetic storm. The bottom X axis shows the GSE coordinates of the spacecraft at various times.

features compared to the ideal MHD simulation at the mesoscale. The Hall MHD simulation, on the other hand, produces significantly more oscillations than observed in multiple time periods.

Since Geotail only observes along a single trajectory, it cannot provide insight into the full dynamics of the magnetotail. To compare the different models, we plot results on 2-D surfaces. Figure 8 shows the magnetosphere simulation results from three models at the same time, 2011-08-05 19:40:00. Figures 8a1–8c1 show the

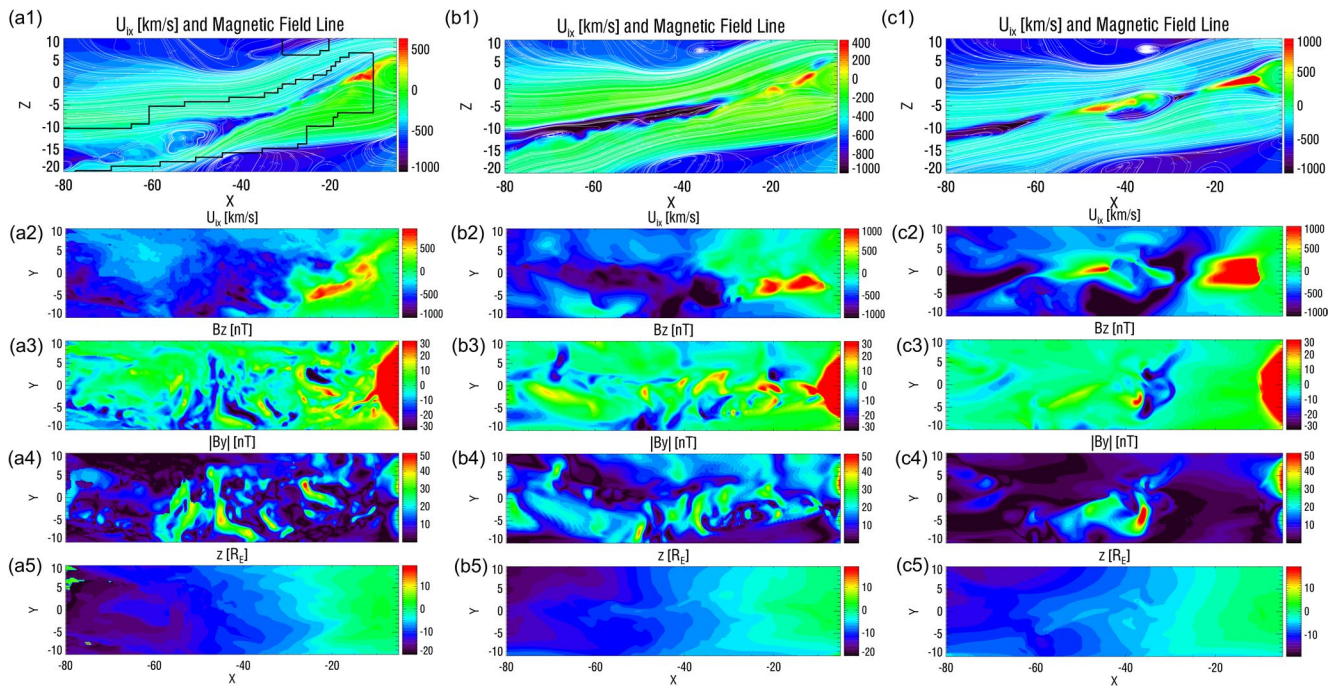


Figure 8. (a1) The x component of the ion bulk velocity u_{ix} and magnetic field lines on the meridional plane from the magnetohydrodynamic with adaptively embedded particle-in-cell (MHD-AEPIC) simulation. The black line shows the boundary of the active PIC region. (a2) u_{ix} on the current sheet surface projected on the x - y plane. (a3) The contour plot of the B_z on the current sheet surface, color saturated at ± 30 nT. (a4) The absolute value of B_y on the current sheet surface. A pair of positive and negative B_z along with a core B_y indicates a flux rope structure. (a5) The z coordinate of the current sheet surface in the unit of R_E . (b1)–(b5) are same quantities from the Hall MHD and (c1)–(c5) are from the ideal MHD simulation. All snapshots are taken at the same time 2011-08-05 19:40:00.

x component of the ion bulk velocity and magnetic field lines in the meridional plane ($-80 R_E < x < -5 R_E$ and $-20 R_E < z < 10 R_E$) from MHD-AEPIC, Hall MHD, and ideal MHD simulations, respectively. The global configurations of the magnetosphere share a lot of similarities but there are several differences as well. All three models give a southward tilted magnetotail that is compressed most in the z direction at around $x = -40 R_E$ as a result of the IMF structure. In terms of the reconnection feature, all three models generate X-lines in the tail current sheet at around $x = -20 R_E$ and $z = -5 R_E$. Diverging reconnection ion jets are generated at the major X-line for all three models.

To analyze physical quantities in the current sheet better, we extract the quantities along a surface where $B_x = 0$ and project this surface to the $x - y$ plane for plotting. The bottom row in Figure 8 shows the z coordinate of the center of the current sheet. The structure is similar as in the meridional plane plots: the current sheets are at $z \approx 0$ near Earth and at $z \approx -15 R_E$ at the far tail for MHD-AEPIC and Hall MHD models, while $z \approx -12 R_E$ for ideal MHD. Figures 8a2–8c2 show the ion bulk flow speed on the current sheet surface. There are significant differences among the three models in the earthward ion flow structures. For ideal MHD, the earthward ion flow is distributed roughly symmetrically at $-3 R_E < y < 3 R_E$. The earthward ion jet generated by Hall MHD can only be observed on the dawn side at $-5 R_E < y < 0$. The MHD-AEPIC simulation produces an earthward ion jet both on the dawn and dusk sides. However, the ion jet on the dawn side is further away from the earth than the jets on the dusk side. Also, the earthward ion jets can be observed from $-5 R_E$ to $7 R_E$ in the y direction, which agrees with the observations that earthward flows are observed at a wide range of y values (Angelopoulos et al., 1994).

Although the earthward ion flow from MHD-AEPIC is different from pure MHD models, the similar magnetic field structure and current sheet position indicate that these snapshots from different models represent the same physical state of the magnetosphere. Hence, it is valid to examine the flux rope features based on these results. As first proposed to be formed in Earth's magnetotail (Schindler, 1974), magnetic flux ropes are reported to be closely related to magnetic reconnection by various observations and simulations (Daughton et al., 2006; Hones Jr et al., 1984; Markidis et al., 2013; Slavin et al., 1989). The observational characteristics of the flux ropes are a pair of positive and negative B_z signatures with a core magnetic field B_y in between. Hence, we plot the B_z and

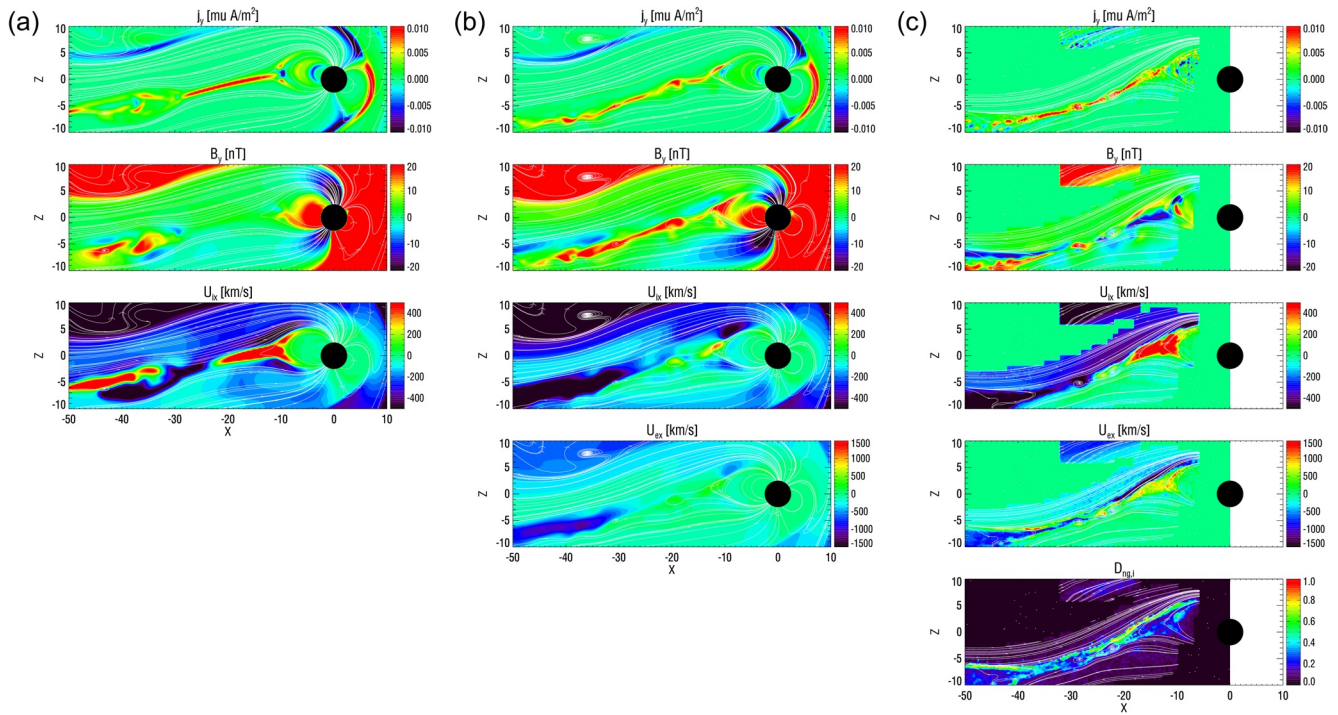


Figure 9. (a) The current density j_y , out-of-plane magnetic field B_y and ion bulk velocity in the x direction U_{ix} from the ideal magnetohydrodynamic (MHD) model near the reconnection X-line. (b) Same physical quantities as panel (a) from the Hall MHD model with an extra electron bulk velocity in the x direction U_{ex} calculated from the current. (c) Same physical quantities as panel (b) from the MHD-AEPIC model with an extra ion nongyrotropy measure $D_{ng,i}$ defined by Aunai et al. (2013). Only the data from the active PIC region are shown in column (c), identified by the area covered with magnetic field lines. All snapshots are taken at the same time 2011-08-05 19:40:00.

$|B_y|$ components on the current sheet surface in Figures 8a–8c (2–3). Panels (c3) and (c4) show only one flux rope at $-40 R_E$ and there is no evidence indicating that a flux rope exists at the near earth plasma sheet from $-40 R_E$ to Earth based on the ideal MHD model results. The Hall MHD and MHD-AEPIC give very different flux rope occurrence (Figures 8a and 8b (3–4)) from ideal MHD. In addition to the moving directions of the flux ropes, the diameter of the flux ropes also varies: the earthward flux ropes are observed as smaller ones. This difference has been reported in a thorough analysis of Geotail observations (Slavin et al., 2003). By examining the flux ropes as a mesoscale feature, we can conclude that by modeling the reconnection physics better, the MHD-AEPIC and Hall MHD simulations produce more flux ropes in the magnetotail than ideal MHD as well as distinguish two types of the flux ropes. However, there is no evidence supporting that MHD-AEPIC can produce better mesoscale features than Hall MHD. This could be the case because the spatial scale of the flux ropes is much larger than the kinetic scale that the PIC model is resolving.

Figure 9 shows different physical quantities near the reconnection X-line at the same time as Figure 8. Panel (a) shows the current density of the current sheet j_y , the out-of-plane magnetic field B_y and the ion bulk velocity U_{ix} from the ideal MHD model. The current sheet is smooth and narrow around the X-line. The simulation produces a diverging ion outflow as expected. There is no significant B_y near the reconnection site due to the lack of Hall physics in the ideal MHD model. Panel (b) shows the same quantities as Panel (a) for the Hall MHD model. In addition, the bottom plot shows the electron velocity in the x direction calculated from the ion bulk velocity and the Hall velocity as $u_{ex} = u_{ix} - j_x/(ne)$. Different from the current sheet in the ideal MHD model, the current sheet in the Hall MHD simulation breaks up at multiple locations. There are strong B_y signatures in the Hall MHD simulation as expected from Hall physics, although the presence of the nonuniform guide field somewhat distorts the classical quadrupolar structure. The diverging ion bulk flow is very similar to the diverging electron flow, because the j_x component of the current is weak. Panel (c) shows the same quantities as Panel (b) from the MHD-AEPIC model with an extra ion nongyrotropy measure $D_{ng,i}$. The current sheet in the MHD-AEPIC simulation also forms multiple flux ropes similar to the Hall MHD results. The MHD-AEPIC model also generates the Hall magnetic field B_y . The ion and electron velocities from the MHD-AEPIC show very clear inflow and outflow

features that are quite different from the Hall MHD solution. While both ideal and Hall MHD assume isotropic pressures, the PIC simulation allows a general pressure tensor with anisotropy and even nongyrotopy (nonzero off-diagonal terms). Aunai et al. (2013) define the nongyrotopy measure as

$$D_{ng} = 2 \frac{\sqrt{P_{12}^2 + P_{23}^2 + P_{13}^2}}{P_{11} + P_{22} + P_{33}} \quad (14)$$

Here, P_{ij} are the pressure tensor components in the local magnetic field aligned coordinate system. The D_{ng} quantity produced by the MHD-AEPIC model shows that the ion nongyrotopy increases near the X-line. In conclusion, both Hall MHD and MHD-AEPIC generate more features than the ideal MHD model. The MHD-AEPIC and the Hall MHD models generate similar Hall magnetic field structures and current sheet features. The MHD-AEPIC model generates distinct ion and electron bulk flows, as well as the nongyrotopy pressure distribution near the X-line.

3.5. Kinetic Scale: Electron Velocity Distribution Function

In this subsection, we will demonstrate that the kinetic physics at the reconnection site is also properly captured by the MHD-AEPIC model. The magnetic reconnection is regarded as one of the most fundamental physical processes to transfer energy from the magnetic field to plasma. Since the launch of the Magnetospheric Multi-scale (MMS) mission (Burch et al., 2016), magnetic reconnection has been observed at the electron scale during multiple satellite crossings of the electron diffusion region (EDR) (Webster et al., 2018). The EDR encounters exhibit electron nongyrotopy, which can be recognized by crescent-shaped electron distributions (Torbert et al., 2018).

Figure 10 compares the MHD-AEPIC simulation with MMS observations (Hwang et al., 2019). Panel (a) is a contour plot of ion bulk velocity in the meridional plane at $t = 2011-08-05$ 23:20:00. The ion jets, a clear signature of magnetic reconnection, are shown by the blue and red colors. The dashed white line near the X-line, which is rotated by about 13.3° , is the L direction of the local reconnection coordinate system. We also found that the M axis is aligned with the y axis in GSM. So, the LMN coordinate vectors for this reconnection event are $L = (0.972, 0, 0.233)$, $M = (0, 1, 0)$ and $N = (-0.233, 0, 0.972)$. The electron velocities are shown in the LMN coordinate system to allow a direct comparison with the MMS observations. Panels (b) and (d) show the electron velocity distribution functions (VDF) from the model and the MMS observation. The simulation VDF of the electrons is collected inside an ellipsoid region centered at $(-30.6, 0.5, -0.9) R_E$ with principle semi-axes $(0.3, 2.5, 0.3) R_E$ in the (x, y, z) directions, respectively. The red circle in panel (a) labeled by B is the cross section of the ellipsoid with the meridional plane. The choice of the ellipsoid shape is based on panel (c) that shows where the MMS observations were taken with respect to the reconnection site according to Figure 2 by Hwang et al. (2019). The MMS3 observations of the electron VDF (Hwang et al., 2019) at the location $(-18.1, 7.30, 0.66) R_E$ are shown in panel (d). Although the simulation and observation are not from the same event and the EDR is not at the same position in GSM coordinates, the electron data are collected at a similar location relative to the X-line and the velocity components are all projected to the LMN coordinates (see panels (a) and (c)).

This suggests that we can directly compare the two VDF plots in panels (b) and (d), and they indeed agree very well. The agreement is not only qualitative but in fact quantitative. Since the ion-electron mass ratio is 100, the simulated electron velocity is multiplied by $\sqrt{\frac{m_{i,real}}{m_{e,real}} / \frac{m_{i,simulation}}{m_{e,simulation}}} \approx \sqrt{18.36} \approx 4.28$ to be comparable with the observations. In both panels the velocity distribution extends to $\pm 40,000$ km/s in the N direction and $(-40,000, +20,000)$ km/s in the M direction. A non-Maxwellian core distribution can also be clearly identified in both panels at $(-20,000 \text{ km/s} < v_y < 10,000 \text{ km/s})$ and $|v_z| < 10,000 \text{ km/s}$. In addition to the EDR, we also collected electrons inside two other ellipsoids at the inflow (labeled by A) and outflow (labeled by C) regions. The semi-axes of these two ellipsoids are the same as before while the centers of the ellipsoids are $(-28.5, 1.5, 0.5) R_E$ and $(-33.0, 1.5, -1.0) R_E$ in the (x, y, z) directions, respectively. Panels (e) and (f) show the electron VDF in $L - N$ and $L - M$ coordinates, and the distribution can be characterized as a bidirectional beam distribution (Asano et al., 2008). The distribution functions at the outflow region in panels (g) and (h) are almost circles with shifted centers indicating the direction of the bulk velocities. The distribution functions from the inflow and outflow also agree very well with the existing theories (Egedal et al., 2010; Pritchett, 2006). Hence, we can conclude that an

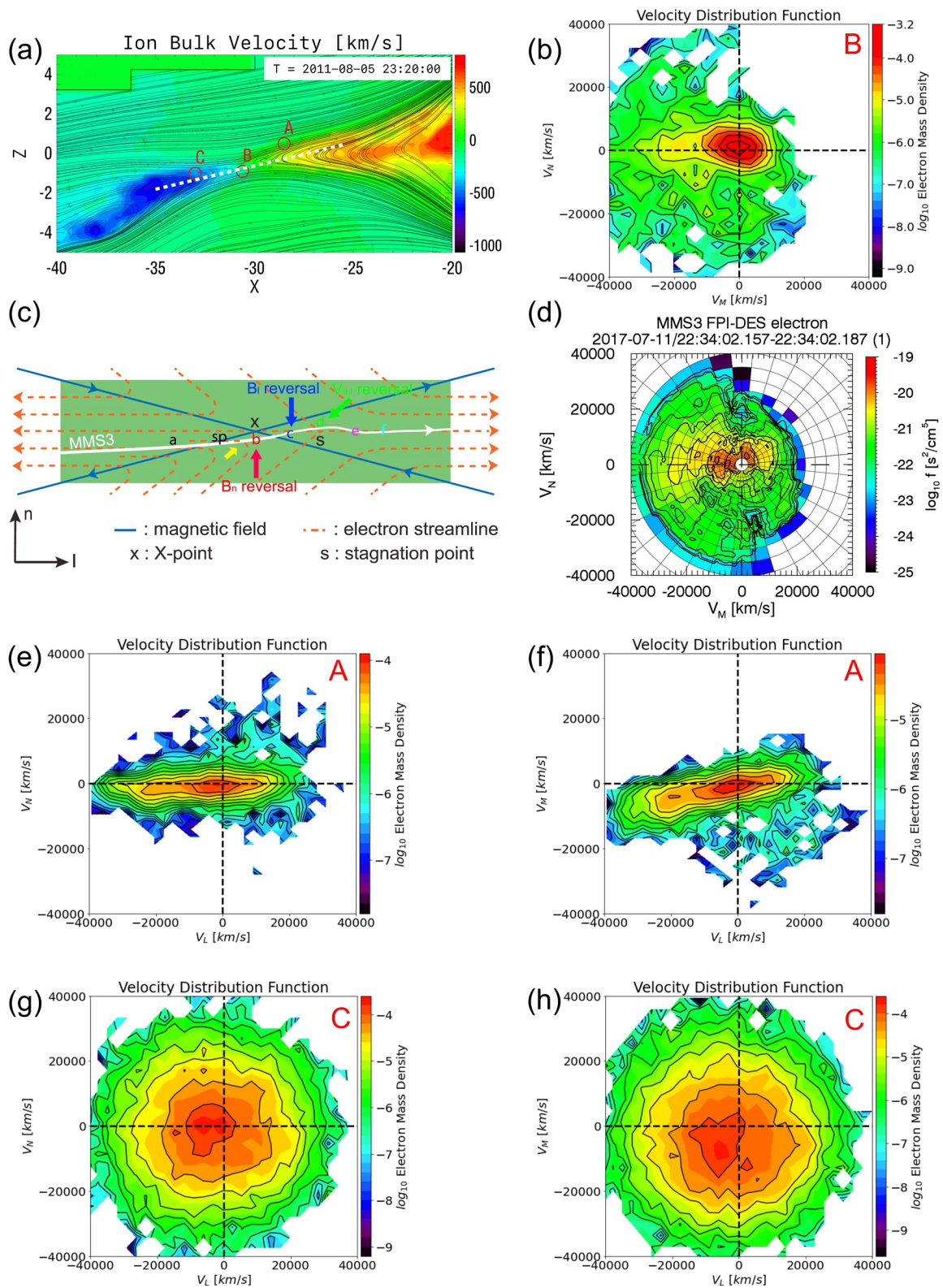


Figure 10.

MHD-AEPIC global simulation can generate electron phase space distributions that are very close to the MMS observations, and reproduces the main features of reconnection physics even at the electron scales.

4. Conclusions and Discussions

In this paper, we introduced a newly developed magnetohydrodynamic with adaptively embedded particle-in-cell (MHD-AEPIC) model. The MHD-AEPIC allows PIC grid cells to be turned on and off during the simulation based on the physical criteria provided. Different from the previous MHD-EPIC model, which requires a fixed Cartesian box to cover the PIC region, the MHD-AEPIC model enables PIC regions moving with the reconnection sites to save computational resources substantially. During the main phase of the storm, from $t = 2011-08-06\ 00:05:00$ to $t = 2011-08-06\ 02:54:00$, when the volume of the PIC domain is about $12,000 R_E^3$. The relative timings are the following: 72.72% of CPU time is used on FLEKS, 13.26% is for BATS-R-US, and 10.35% is taken by the coupling between FLEKS and BATS-R-US. The rest 3.67% of CPU time is consumed by RIM, RCM, and the overhead of the SWMF. For the entire 16-hr geomagnetic storm simulation, the total wall time is 256.29 hr on 5600 CPU cores.

We also introduced three physics-based criteria to identify the reconnection regions in the magnetotail. To demonstrate the feasibility of the MHD-AEPIC model, we have performed a geomagnetic storm event simulation with kinetic physics embedded for the first time. It remains to be determined whether kinetic physics can play a more important role in other events, including but not limited to substorms. The flapping motion of the magnetotail current sheet during the geomagnetic storm highlights the advantage of the adaptation feature of the MHD-AEPIC model.

We have also simulated the same event using Hall MHD and ideal MHD models and compared the three models at multiple physical scales. We examined the global scale features by comparing the SYM-H and SME indexes, which reflect the equatorial and auroral region disturbances, respectively. All three models properly capture the global scale disturbances such as the main phase of the storm or the increase of the auroral electrojet. However, all three models fail to produce the strongest intensity for the geomagnetic indices. Hence, no significant difference is found among the three different models at the global scale for this event. This indicates that the GM configuration from the three models are very close, and the kinetic model embedded in the magnetotail does not improve the global scale feature for this geomagnetic storm. Whether this trend persists for other storms, especially extreme events, is still to be investigated.

We analyze the mesoscale features by comparing the magnetic field components and ion profiles between the Geotail observation and the simulations. All three models show fairly good agreement with the Geotail observations; however, none of the three models can match all features such as all the current sheet crossing or flux rope signatures. The Hall MHD simulation shows more oscillations than observed during a few time periods. In this storm event, MHD-AEPIC and ideal MHD models produce similar agreement with the in situ observations of Geotail.

In addition to comparing with the Geotail observations, we also compare the three models with respect to flux rope structures in the current sheet. Only one major flux rope can be observed from the ideal MHD simulation at the selected time, while Hall MHD and MHD-AEPIC can produce flux ropes at a wider range in the dawn-dusk direction. The difference of two types of the flux ropes, earthward with smaller spatial scale and tailward with a larger spatial scale, is also illustrated by the MHD-AEPIC simulations, in agreement with several observations (Slavin et al., 2003).

The electron scale kinetic physics is well reproduced by the MHD-AEPIC model. We collect electron macro-particle velocities at the same side of the EDR as the MMS3 satellite did (Hwang et al., 2019). The VDF show excellent agreement between the simulation and the MMS3 observation. This demonstrates that MHD-AEPIC can properly produce the electron scale features within a single self-consistent global model while simulating a complete geomagnetic storm event. In this particular simulation, including the kinetic reconnection

Figure 10. (a) The contour plot of the ion bulk velocity overlapped with magnetic field lines. The 2D cut is taken on the meridional plane. The three red circles are the position where the electrons for the velocity distribution functions (VDF) are collected. (a) Inflow region, (b) electron diffusion region, and (c) outflow region. The white dashed line with a notice that some area at upper left is not covered by particle-in-cell (PIC), which illustrates the AEPIC feature. (b) The electron VDF from the simulation, colored in electron mass density in log scale. (c) A sketch (Figure 1b in Hwang et al. (2019)) demonstrating possible magnetic field geometries. The white curve represents a possible MMS3 trajectory. The electron VDF in (d) is taken at the position b pointed by a red arrow. (d) MMS3 observation (Figure 2c in Hwang et al. (2019)). (e)–(f) The electron VDF taken at the inflow region. (g)–(h) The electron VDF taken at the outflow region.

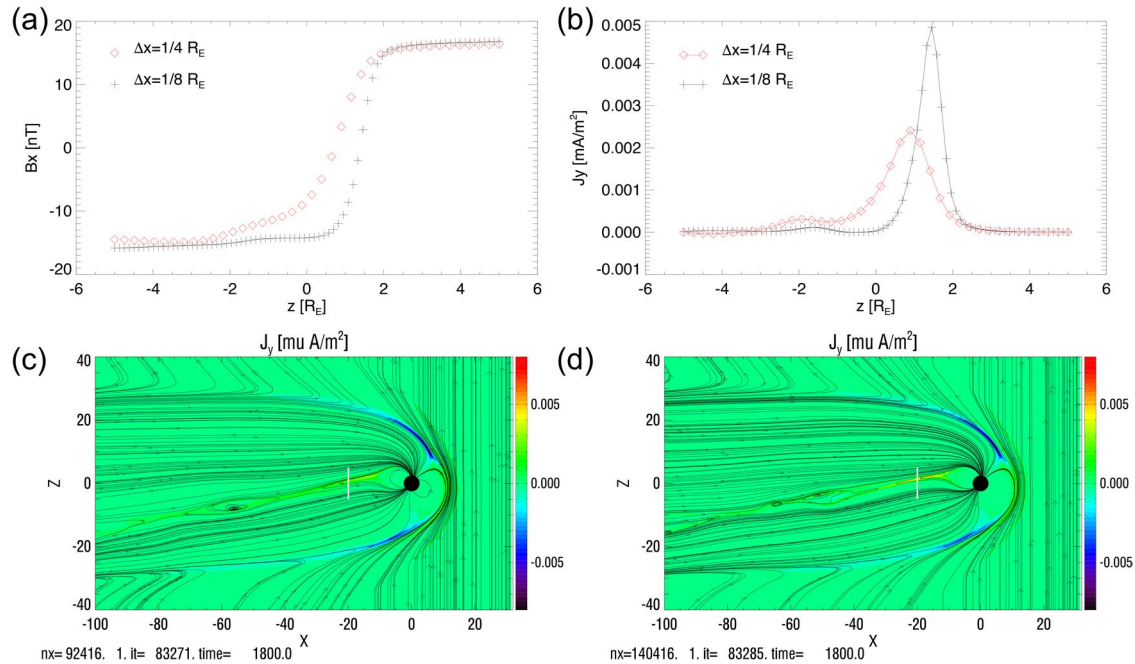


Figure 11. (a) The B_x profiles across the current sheet from two simulations with different grid resolutions in the magnetotail. The profiles are taken along the $x = -20 R_E$ and $y = 0$ line from $z = -5 R_E$ to $5 R_E$. The symbols show the discrete values at the grid cell centers. (b) The J_y current profiles taken at the same position as B_x in panel (a). (c) The meridional cut of the simulation domain with J_y and magnetic field lines for a $1/4 R_E$ grid resolution in the magnetotail. (d) Same physical quantities as panel (c) but with a $1/8 R_E$ grid resolution in the magnetotail. Two snapshots are taken at the same time, 2011-08-05 15:30:00.

physics does not improve agreement with observations at meso- and global scales. This suggests that in this storm event, the magnetosphere is mostly driven by the external solar wind and IMF and not by the internal reconnection dynamics.

It is to be investigated if the kinetic physics can have a more pronounced influence on the physical condition of the magnetosphere when the external drivers are relatively constant. Another important question is to compare the impact of kinetic versus numerical reconnection during extreme events. In addition to studying Earth's magnetosphere, we also expect the novel MHD-AEPIC model will find its applications in various collisionless plasma systems that form small regions where kinetic effects are important inside a large spatial domain.

Appendix A: Reconnection Due To Numerical Resistivity

It is a common practice to rely on numerical resistivity to mimic reconnection physics in global ideal and Hall magnetohydrodynamic (MHD) simulations. Analytic solutions of ideal MHD obey the frozen-in condition: the magnetic flux through a surface co-moving with the plasma (i.e., the ion fluid) does not change. For Hall MHD, the magnetic flux is frozen into the motion of the electron fluid. A consequence of the frozen-in condition is that if two plasma elements are connected by a field line, then they remain connected forever, which means that magnetic reconnection cannot take place.

In reality, and also in the kinetic PIC model, the electrons and ions can “detach” from the magnetic field lines in the ion and electron diffusion regions (EDR), respectively. In effect, this allows the magnetic field lines to reconnect inside the EDR where the frozen in condition does not apply. The simplest mathematical description of this process is adding an Ohmic resistive term $\eta \mathbf{j}$ into the induction equation:

$$\frac{\partial \mathbf{B}}{\partial t} = -\nabla \times [-\mathbf{u}_e \times \mathbf{B} + \eta \mathbf{j}] \quad (\text{A1})$$

For magnetic diffusivity $\eta' = \eta/\mu_0$ one can write this as

$$\frac{\partial \mathbf{B}}{\partial t} = -\nabla \times [-\mathbf{u}_e \times \mathbf{B}] - \nabla \times (\eta' \nabla \times \mathbf{B}) \quad (\text{A2})$$

where we used $\mathbf{j} = (1/\mu_0)\nabla \times \mathbf{B}$ and assumed that η is not constant in space in general. The usual argument in favor of using the ideal MHD model is that numerical resistivity will behave similarly to the diffusive term $\nabla \times (\eta' \nabla \times \mathbf{B})$ and indeed, numerical experiments show that magnetic reconnection remains a robust feature of ideal MHD simulations. On the other hand, one would expect numerical diffusion to go to zero with increased grid resolution, which implies that reconnection should disappear from a well-resolved solution. In this appendix, we take a closer look at resolving this contradiction for 1D geometry and provide arguments for 3D geometry.

The main argument is that an ideal MHD reconnecting current sheet behaves like a discontinuity and therefore, the derivatives of the solution across the current sheet do not converge to a finite value. In particular, the current density, obtained from the derivative of the magnetic field, goes to infinity as the grid resolution is increased, while the numerical diffusion goes to zero. Their product, which determines the reconnection rate, remains finite. Although it is still an open question, the Axford Conjecture (Axford, 1984; Gonzalez et al., 2016) suggests that the global time averaged reconnection rate is predominantly set by the external solar wind and IMF driver. On the dayside, the solar wind brings in magnetic flux at a rate of $lu_x|B_z$. A fraction of this flux will reconnect at the dayside magnetopause for $B_z < 0$. For a time period that is much longer than substorms, since the magnetic flux attached to Earth cannot grow without bound, there has to be a matching reconnection rate in the magnetotail.

We now look in more detail into how the numerical scheme actually achieves this. For finite volume methods solving the

$$\frac{\partial U}{\partial t} + \nabla \cdot \mathbf{F} = 0 \quad (\text{A3})$$

equation, the numerical flux is calculated at the cell interfaces, and it depends on the right and left states U^R and U^L extrapolated from the right and left directions, respectively, and the characteristic wave speeds. The Lax-Friedrichs flux is the simplest example:

$$F^{LF} = \frac{F(U^R) + F(U^L)}{2} - \frac{1}{2} \lambda_{\max} (U^R - U^L) \quad (\text{A4})$$

where F is the physical flux function. The first term contains the physical flux as the average of $F(U^R)$ and $F(U^L)$. The second term introduces numerical diffusion to preserve the monotonicity of the numerical solution. The numerical diffusion is proportional to the fastest wave speed λ_{\max} corresponding to the fast magnetosonic wave in ideal MHD. The $U^R - U^L$ difference is some fraction of the difference between the cell center values on the two sides of the cell:

$$(U^R - U^L)_f = \alpha_f (U_{k+1} - U_k) \quad (\text{A5})$$

Here f represents the index of the cell face between cells indexed by k and $k + 1$. The fraction $0 \leq \alpha_f \leq 1$ depends on the numerical scheme. For a first order scheme, $\alpha_f = 1$. For a higher order scheme, the fraction depends on the limiters used in the algorithm and the differences of U in neighboring cells.

For sake of simplicity, let us consider a current sheet parallel to the $X - Y$ plane and assume that B_x changes the sign across the current sheet as we move in the Z direction. The physical flux function in the Z direction is $F = v_z B_x - v_x B_z$. The numerical flux function at the cell interface f is

$$F_f^{LF} = \frac{F(U_f^R) + F(U_f^L)}{2} - \frac{1}{2} \lambda_{\max, f} \alpha_f (B_{x, k+1} - B_{x, k}) \quad (\text{A6})$$

The numerical diffusive part of the flux can be written as

$$F_f^{\text{diff}} = - \frac{\lambda_{\max, f} \alpha_f \Delta z}{2} \frac{B_{x, k+1} - B_{x, k}}{\Delta z} \quad (\text{A7})$$

which is a numerical approximation of $\eta' \partial_z B_x$ with the numerical diffusivity

$$\eta' = \frac{\lambda_{\max, f} \alpha_f \Delta z}{2} \quad (\text{A8})$$

Indeed in the 1D case with $\partial_y = \partial_z = 0$, the last term in Equation A2 simplifies to

$$-\nabla \times (\eta' \nabla \times \mathbf{B}) = \frac{\partial}{\partial z} \left(\eta' \frac{\partial \mathbf{B}}{\partial z} \right) \quad (\text{A9})$$

which is equivalent to the negative divergence of the numerical flux in Equation A7.

For a smooth solution, $\partial_z B_x$ converges to a finite value as the grid is refined, while η' converges to zero because $\Delta z \rightarrow 0$. For a discontinuous solution, however, the difference $B_{x,k+1} - B_{x,k}$ as well as $\lambda_{\text{max},f}$ and α_f all become independent of the grid resolution as $\Delta z \rightarrow 0$. This is a direct consequence of the fact that neither the ideal MHD equations nor the numerical scheme has any intrinsic length scale other than the grid cell size. This means that the current sheet will be resolved with a fixed number of grid points following a fixed numerical profile (a series of the discrete values $B_{x,k}$ across the current sheet) independent of the grid resolution for a small enough Δz . Therefore the numerical reconnection rate will converge to a finite value, determined predominantly by the external conditions (the external field $B_x^{\pm \text{ext}}$ and the converging velocity $u_z^{\pm \text{ext}}$ outside the current sheet), instead of zero. In physical terms, the numerical resistivity η' goes to 0, but the current density $(1/\mu_0)\Delta B_x/\Delta z$ goes to infinity and their product remains finite.

The maximum possible numerical reconnection rate is $\lambda_{\text{max},f}|B^{+\text{ext}} - B^{-\text{ext}}|/2$ corresponding to a current sheet where the magnetic field jumps from $B_x^L = B_{x,k} = B_x^{\text{ext}}$ to $B_x^R = B_{x,k+1} = B_x^{\text{ext}}$ across a single cell face, and $\lambda_{\text{max},f}$ is the maximum (or average) of the fast magnetosonic speeds taken at the two cell centers next to the face. The fraction α_f is 1 at this interface, independent of the nominal order of the scheme, because all schemes drop to the first order at this type of numerical discontinuity due to the limiters. This maximum numerical reconnection rate far exceeds the typical physical reconnection rate $\approx 0.1v_A|B^{\text{ext}}|$, where v_A is the Alfvén speed, found in PIC simulations. Note that while the 1D reconnection geometry looks like a Sweet-Parker type reconnection, the numerical resistivity can far exceed the physical collisional resistivity, so it can be fast. The actual numerical profile realized by the numerical scheme will have multiple points across the current sheet, resulting in a lower numerical diffusion rate than the theoretical maximum. In a 2 or 3 dimensional system, the global reconnection rate will depend on many factors, including the presence of Hall physics, which has a major impact on the structure of the reconnection site (Birni et al., 2001) and the achievable reconnection rate.

Figure 11 shows that these theoretical consideration are indeed valid in a complicated 3D magnetosphere simulation. We have performed two ideal MHD simulations with $\Delta x = 1/4 R_E$ and $1/8 R_E$ grid resolutions in the magnetotail, respectively. We compare the numerical solution across the current sheet at the same place and same time. As the figure shows, the number of grid cells, represented by the symbols, across the current sheet and the magnetic field values at the cell centers are essentially the same in the two simulations. The only change is the physical distance between the cells, which is reduced by a factor of 2 on the finer grid. As a result, the current density is twice higher, while the numerical dissipation rate is half of those obtained on the coarser grid. In the end, the reconnection rate is essentially the same in the two simulations, which results in essentially the same global solution.

Data Availability Statement

The Geotail data are publicly available at Data ARchives and Transmission System (DARTS) of Institute of Space and Astronautical Science (ISAS) (<https://darts.isas.jaxa.jp>). The MMS observation plot is acquired with consent from Dr. K.-J. Hwang (jhwang@swri.edu). The SWMF code (including BATS-R-US and FLEKS) is publicly available through the csem.engin.umich.edu/tools/swmf website after registration. The simulation output and scripts used for generating figures in this paper can be obtained online (<https://doi.org/10.7302/xtvh-tq17>) through the University of Michigan's Deep Blue Data repository, which is specifically designed for U-M researchers to share their research data and to ensure its long-term viability.

References

- Angelopoulos, V., Kennel, C. F., Coroniti, F. V., Pellat, R., Kivelson, M. G., Walker, R. J., et al. (1994). Statistical characteristics of bursty bulk flow events. *Journal of Geophysical Research*, 99(21), 257. <https://doi.org/10.1029/94ja01263>
- Asano, Y., Nakamura, R., Shinohara, I., Fujimoto, M., Takada, T., Baumjohann, W., et al. (2008). Electron flat-top distributions around the magnetic reconnection region. *Journal of Geophysical Research*, 113(A1), A01207. <https://doi.org/10.1029/2007ja012461>
- Aunai, N., Hesse, M., & Kuznetsova, M. (2013). Electron nongyrotropy in the context of collisionless magnetic reconnection. *Physics of Plasmas*, 20(9), 092903. <https://doi.org/10.1063/1.4820953>
- Axford, W. (1984). Magnetic field reconnection. *American Geophysical Union Geophysical Monograph Series*, 30, 1–8.

Acknowledgments

We thank Dr. Qusai Al Shidi at the University of Michigan for the script calculating the SME index using interpolated virtual magnetometer data from BATS-R-US. This work was primarily supported by NSF PRE-EVENTS Grant No. 1663800. We also acknowledge support from the NASA DRIVE Center at the University of Michigan under grant NASA 80NSSC20K0600. We acknowledge the use of computational resources provided by an NSF LRAC allocation at the Texas Advanced Computing Center (TACC) at The University of Texas at Austin.

- Bergin, A., Chapman, S. C., & Gjerloev, J. W. (2020). AE, D_{ST}, and their SuperMAG counterparts: The effect of improved spatial resolution in geomagnetic indices. *Journal of Geophysical Research: Space Physics*, 125(5), e2020JA027828. <https://doi.org/10.1029/2020ja027828>
- Birn, J., Drake, J. F., Shay, M. A., Rogers, B. N., Denton, R. E., Hesse, M., et al. (2001). Geospace environmental modeling (GEM) magnetic reconnection challenge. *Journal of Geophysical Research*, 106(A3), 3715–3720. <https://doi.org/10.1029/1999JA900449>
- Birn, J., Hesse, M., & Schindler, K. (2006). Entropy conservation in simulations of magnetic reconnection. *Physics of Plasmas*, 13(9), 092117. <https://doi.org/10.1063/1.2349440>
- Birn, J., Hesse, M., Schindler, K., & Zaharia, S. (2009). Role of entropy in magnetotail dynamics. *Journal of Geophysical Research*, 114(A9), A00D03. <https://doi.org/10.1029/2008ja014015>
- Brecht, S., Lyon, J., Fedder, J., & Hain, K. (1981). A simulation study of east-west IMF effects on the magnetosphere. *Geophysical Research Letters*, 8(4), 397–400. <https://doi.org/10.1029/gl008i004p00397>
- Brecht, S., Lyon, J., Fedder, J., & Hain, K. (1982). A time-dependent three-dimensional simulation of the Earth's magnetosphere: Reconnection events. *Journal of Geophysical Research*, 87(A8), 6098–6108. <https://doi.org/10.1029/ja087ia08p06098>
- Burch, J. L., Torbert, R. B., Phan, T. D., Chen, L.-J., Moore, T. E., Ergun, R. E., et al. (2016). Electron-scale measurements of magnetic reconnection in space. *Science*, 352, 6290. <https://doi.org/10.1126/science.aaf2939>
- Chen, L.-J., Hesse, M., Wang, S., Gershman, D., Ergun, R., Pollock, C., et al. (2016). Electron energization and mixing observed by MMS in the vicinity of an electron diffusion region during magnetopause reconnection. *Geophysical Research Letters*, 43(12), 6036–6043. <https://doi.org/10.1002/2016gl069215>
- Chen, Y., & Tóth, G. (2019). Gauss's law satisfying energy-conserving semi-implicit particle-in-cell method. *Journal of Computational Physics*, 386, 632–652. <https://doi.org/10.1016/j.jcp.2019.02.032>
- Chen, Y., Tóth, G., Cassak, P., Jia, X., Gombosi, T. I., Slavin, J., et al. (2017). Global three-dimensional simulation of Earth's dayside reconnection using a two-way coupled magnetohydrodynamics with embedded particle-in-cell model: Initial results. *Journal of Geophysical Research*, 122(10), 10318. <https://doi.org/10.1002/2017JA024186>
- Chen, Y., Tóth, G., Jia, X., Slavin, J. A., Sun, W., Markidis, S., et al. (2019). Studying dawn-dusk asymmetries of Mercury's magnetotail using MHD-EPIC simulations. *Journal of Geophysical Research: Space Physics*, 124(11), 8954–8973. <https://doi.org/10.1029/2019ja026840>
- Chen, Y., Toth, G., Zhou, H., & Wang, X. (2021). Fleks: A flexible particle-in-cell code for multi-scale plasma simulations. *Earth and Space Science Open Archive*. <https://doi.org/10.1002/essoar.10508070.1>
- Daldrorf, L. K. S., Tóth, G., Gombosi, T. I., Lapenta, G., Amaya, J., Markidis, S., & Brackbill, J. U. (2014). Two-way coupling of a global Hall magnetohydrodynamics model with a local implicit particle-in-Cell model. *Journal of Computational Physics*, 268, 236–254. <https://doi.org/10.1016/j.jcp.2014.03.009>
- Daughton, W., Scudder, J., & Karimabadi, H. (2006). Fully kinetic simulations of undriven magnetic reconnection with open boundary conditions. *Physics of Plasmas*, 13(7), 072101. <https://doi.org/10.1063/1.2218817>
- Davis, T. N., & Sugiura, M. (1966). Auroral electrojet activity index AE and its universal time variations. *Journal of Geophysical Research*, 71(3), 785–801. <https://doi.org/10.1029/jz071i003p00785>
- Dedner, A., Kemm, F., Kröner, D., Munz, C., Schnitzer, T., & Wesenberg, M. (2003). Hyperbolic divergence cleaning for the MHD equations. *Journal of Computational Physics*, 175(2), 645–673. <https://doi.org/10.1006/jcph.2001.6961>
- De Zeeuw, D., Sazykin, S., Wolf, R., Gombosi, T., Ridley, A., & Tóth, G. (2004). Coupling of a global MHD code and an inner magnetosphere model: Initial results. *Journal of Geophysical Research*, 109(A12), 219. <https://doi.org/10.1029/2003JA010366>
- Egedal, J., Lê, A., Katz, N., Chen, L.-J., Lefebvre, B., Daughton, W., & Fazakerley, A. (2010). Cluster observations of bidirectional beams caused by electron trapping during antiparallel reconnection. *Journal of Geophysical Research*, 115(A3), A03214. <https://doi.org/10.1029/2009ja014650>
- Ganushkina, N., Jaynes, A., & Liemohn, M. (2017). Space weather effects produced by the ring current particles. *Space Science Reviews*, 212(3), 1315–1344. <https://doi.org/10.1007/s11214-017-0412-2>
- Gao, Y. (2012). Comparing the cross polar cap potentials measured by SuperDARN and AMIE during saturation intervals. *Journal of Geophysical Research*, 117(A8), A08325. <https://doi.org/10.1029/2012ja017690>
- Glocer, A., Dorelli, J., Tóth, G., Komar, C. M., & Cassak, P. A. (2016). Separator reconnection at the magnetopause for predominantly northward and southward IMF: Techniques and results. *Journal of Geophysical Research*, 121(1), 140–156. <https://doi.org/10.1002/2015JA021417>
- Glocer, A., Tóth, G., Ma, Y. J., Gombosi, T., Zhang, J.-C., & Kistler, L. M. (2009). Multifluid block-adaptive-tree solar wind roe-type upwind scheme: Magnetospheric composition and dynamics during geomagnetic storms—Initial results. *Journal of Geophysical Research*, 114(A12), A12203. <https://doi.org/10.1029/2009JA014418>
- Gonzalez, W., Parker, E., Mozer, F., Vasyliūnas, V., Pritchett, P., Karimabadi, H., et al. (2016). Fundamental concepts associated with magnetic reconnection. In *Magnetic reconnection* (pp. 1–32). Springer.
- Haiducek, J. D., Welling, D. T., Ganushkina, N. Y., Morley, S. K., & Ozturk, D. S. (2017). SWMF global magnetosphere simulations of January 2005: Geomagnetic indices and cross-polar cap potential. *Space Weather*, 15(12), 1567–1587. <https://doi.org/10.1002/2017sw001695>
- Hairston, M. R., Weimer, D. R., Heelis, R. A., & Rich, F. (1998). Analysis of the ionospheric cross polar cap potential drop and electrostatic potential distribution patterns during the January 1997 CME event using DMSP data. *Journal of Atmospheric and Solar-Terrestrial Physics*, 61(3–4), 195–206. [https://doi.org/10.1016/s1364-6826\(98\)00128-x](https://doi.org/10.1016/s1364-6826(98)00128-x)
- Hones, E., Jr., Birn, J., Baker, D., Bame, S., Feldman, W., McComas, D., et al. (1984). Detailed examination of a plasmoid in the distant magnetotail with ISEE 3. *Geophysical Research Letters*, 11(10), 1046–1049. <https://doi.org/10.1029/gl011i010p01046>
- Hwang, K.-J., Choi, E., Dokgo, K., Burch, J., Sibeck, D., Giles, B., et al. (2019). Electron vorticity indicative of the electron diffusion region of magnetic reconnection. *Geophysical Research Letters*, 46(12), 6287–6296. <https://doi.org/10.1029/2019gl082710>
- Janhunen, P. (1996). GUMICS-3: A global ionosphere-magnetosphere coupling simulation with high ionospheric resolution. In *Proceedings of the ESA 1996 symposium on environment modelling for space-based applications* (pp. 233–239). ESA SP-392.
- Koren, B. (1993). A robust upwind discretisation method for advection, diffusion and source terms. In C. Vreugdenhil & B. Koren (Eds.), *Numerical methods for advection-diffusion problems* (p. 117). Vieweg.
- LeBoeuf, J. N., Tajima, T., Kennel, C. F., & Dawson, J. M. (1981). Global simulations of the three-dimensional magnetosphere. *Geophysical Research Letters*, 8(3), 257–260. <https://doi.org/10.1029/gl008i003p00257>
- Li, X., Guo, F., & Li, H. (2019). Particle acceleration in kinetic simulations of nonrelativistic magnetic reconnection with different ion–electron mass ratios. *The Astrophysical Journal*, 879(1), 5. <https://doi.org/10.3847/1538-4357/ab223b>
- Lotekar, A., Vasko, I., Mozer, F., Hutchinson, I., Artemyev, A., Bale, S., et al. (2020). Multisatellite mms analysis of electron holes in the Earth's magnetotail: Origin, properties, velocity gap, and transverse instability. *Journal of Geophysical Research: Space Physics*, 125(9), e2020JA028066. <https://doi.org/10.1029/2020ja028066>
- Lyon, J., Fedder, J., & Mobarry, C. (2004). The Lyon-Fedder-Mobarry (LFM) global MHD magnetospheric simulation code. *Journal of Atmospheric and Solar-Terrestrial Physics*, 66(15–16), 1333–1350. <https://doi.org/10.1016/j.jastp.2004.03.020>

- Lyon, J. G., Fedder, J., & Huba, J. (1986). The effect of different resistivity models on magnetotail dynamics. *Journal of Geophysical Research*, 91(A7), 8057–8064. <https://doi.org/10.1029/ja091ia07p08057>
- Ma, X., & Otto, A. (2014). Nonadiabatic heating in magnetic reconnection. *Journal of Geophysical Research: Space Physics*, 119(7), 5575–5588. <https://doi.org/10.1002/2014ja019856>
- Ma, Y., Russell, C. T., Toth, G., Chen, Y., Nagy, A. F., Harada, Y., et al. (2018). Reconnection in the Martian magnetotail: Hall-MHD with embedded particle-in-cell simulations. *Journal of Geophysical Research: Space Physics*, 123(5), 3742–3763. <https://doi.org/10.1029/2017ja024729>
- Markidis, S., Henri, P., Lapenta, G., Divin, A., Goldman, M., Newman, D., & Laure, E. (2013). Kinetic simulations of plasmoid chain dynamics. *Physics of Plasmas*, 20(8), 082105. <https://doi.org/10.1063/1.4817286>
- Markidis, S., Lapenta, G., & Uddin, R. (2010). Multi-scale simulations of plasma with iPIC3D. *Mathematics and Computers in Simulation*, 80(7), 1509–1519. <https://doi.org/10.1016/j.matcom.2009.08.038>
- Merkin, V. G., Panov, E. V., Sorathia, K., & Ukhorskiy, A. Y. (2019). Contribution of bursty bulk flows to the global dipolarization of the magnetotail during an isolated substorm. *Journal of Geophysical Research: Space Physics*, 124(11), 8647–8668. <https://doi.org/10.1029/2019ja026872>
- Newell, P., & Gjerloev, J. (2011). Evaluation of SuperMAG auroral electrojet indices as indicators of substorms and auroral power. *Journal of Geophysical Research*, 116(A12), A12211. <https://doi.org/10.1029/2011ja016779>
- Powell, K., Roe, P., Linde, T., Gombosi, T., & De Zeeuw, D. L. (1999). A solution-adaptive upwind scheme for ideal magnetohydrodynamics. *Journal of Computational Physics*, 154(2), 284–309. <https://doi.org/10.1006/jcph.1999.6299>
- Pritchett, P. (2006). Relativistic electron production during driven magnetic reconnection. *Geophysical Research Letters*, 33(13), L13104. <https://doi.org/10.1029/2005gl025267>
- Pulkkinen, A., Rastatter, L., Kuznetova, M., Singer, H., Balch, C., Weimer, D., et al. (2013). Community-wide validation of geospace model ground magnetic field perturbation predictions to support model transition to operations. *Space Weather*, 11(6), 369–385. <https://doi.org/10.1002/swe.20056>
- Raeder, J., Berchem, J., & Ashour-Abdalla, M. (1996). The importance of small scale processes in global MHD simulations: Some numerical experiments. In T. Chang & J. R. Jasperse (Eds.), *The physics of space plasmas* (Vol. 14, p. 403). Cambridge.
- Raeder, J., McPherron, R., Frank, L., Kokubun, S., Lu, G., Mukai, T., et al. (2001). Global simulation of the geospace environment modeling substorm challenge event. *Journal of Geophysical Research*, 106(A1), 281–395. <https://doi.org/10.1029/2000ja000605>
- Raeder, J., Walker, R. J., & Ashour-Abdalla, M. (1995). The structure of the distant geomagnetic tail during long periods of northward IMF. *Geophysical Research Letters*, 22(4), 349–352. <https://doi.org/10.1029/94gl03380>
- Richmond, A., & Kamide, Y. (1988). Mapping electrodynamic features of the high-latitude ionosphere from localized observations: Technique. *Journal of Geophysical Research*, 93(A6), 5741–5759. <https://doi.org/10.1029/ja093ia06p05741>
- Ridley, A., Gombosi, T., & De Zeeuw, D. (2004). Ionospheric control of the magnetosphere: Conductance. *Annales Geophysicae*, 22(2), 567–584. <https://doi.org/10.5194/angeo-22-567-2004>
- Ridley, A. J., & Kihn, E. A. (2004). Polar cap index comparisons with AMIE cross polar cap potential, electric field, and polar cap area. *Geophysical Research Letters*, 31(7), 07801. <https://doi.org/10.1029/2003GL019113>
- Ruohoniemi, J., & Greenwald, R. (1998). The response of high latitude convection to a sudden southward IMF turning. *Geophysical Research Letters*, 25(15), 2913–2916. <https://doi.org/10.1029/98gl02212>
- Schindler, K. (1974). A theory of the substorm mechanism. *Journal of Geophysical Research*, 79(19), 2803–2810. <https://doi.org/10.1029/ja079i019p02803>
- Shou, Y., Y. Shen, V., Chen, Y., Toth, G., & Ganushkina, N. (2021). Magnetohydrodynamic with adaptively embedded particle-in-cell model: MHD-aepic. *Journal of Computational Physics*, 446, 110656. <https://doi.org/10.1016/j.jcp.2021.110656>
- Slavin, J., Baker, D., Craven, J., Elphic, R., Fairfield, D., Frank, L., et al. (1989). CDAW 8 observations of plasmoid signatures in the geomagnetic tail: An assessment. *Journal of Geophysical Research*, 94(A11), 15153–15175. <https://doi.org/10.1029/ja094a11p15153>
- Slavin, J., Lepping, R., Gjerloev, J., Fairfield, D., Hesse, M., Owen, C., & Mukai, T. (2003). Geotail observations of magnetic flux ropes in the plasma sheet. *Journal of Geophysical Research*, 108(A1), SMP-10. <https://doi.org/10.1029/2002ja009557>
- Sokolov, I. V., Timofeev, E. V., Sakai, J. I., & Takayama, K. (1999). On shock capturing schemes using artificial wind. *Shock Waves*, 9(6), 423–426. <https://doi.org/10.1007/s001930050173>
- Toffoletto, F., Sazykin, S., Spiro, R., & Wolf, R. (2003). Inner magnetospheric modeling with the Rice Convection Model. *Space Science Reviews*, 107(1), 175–196. <https://doi.org/10.1023/A:1025532008047>
- Torbert, R., Burch, J., Phan, T., Hesse, M., Argall, M., Shuster, J., et al. (2018). Electron-scale dynamics of symmetric magnetic reconnection diffusion region in space. *Science*, 362(6421), 1391–1395. <https://doi.org/10.1126/science.aat2998>
- Tóth, G., Chen, Y., Gombosi, T. I., Cassak, P., Markidis, S., & Peng, B. (2017). Scaling the ion inertial length and its implications for modeling reconnection in global simulations. *Journal of Geophysical Research*, 122(10), 10336. <https://doi.org/10.1002/2017JA024189>
- Tóth, G., Jia, X., Markidis, S., Peng, B., Chen, Y., Daldorff, L., et al. (2016). Extended magnetohydrodynamics with embedded particle-in-cell simulation of Ganymede's magnetosphere. *Journal of Geophysical Research*, 121(2), 1273–1293. <https://doi.org/10.1002/2015JA021997>
- Tóth, G., Ma, Y. J., & Gombosi, T. I. (2008). Hall magnetohydrodynamics on block adaptive grids. *Journal of Computational Physics*, 227(14), 6967–6984. <https://doi.org/10.1016/j.jcp.2008.04.010>
- Tóth, G., van der Holst, B., Sokolov, I. V., Zeeuw, D. L. D., Gombosi, T. I., Fang, F., et al. (2012). Adaptive numerical algorithms in space weather modeling. *Journal of Computational Physics*, 231(3), 870–903. <https://doi.org/10.1016/j.jcp.2011.02.006>
- Tóth, G., Zeeuw, D. L. D., Gombosi, T. I., Manchester, W. B., Ridley, A. J., Sokolov, I. V., & Roussev, I. I. (2007). Sun to thermosphere simulation of the October 28–30, 2003 storm with the space weather modeling framework. *Space Weather Journal*, 5(6), S06003. <https://doi.org/10.1029/2006SW000272>
- Troshichev, O., Andezen, V., Vennerstrom, S., & Friis-Cristensen, E. (1988). Magnetic activity in the polar cap—A new index. *Planetary and Space Science*, 36(11), 1095–1102. [https://doi.org/10.1016/0032-0633\(88\)90063-3](https://doi.org/10.1016/0032-0633(88)90063-3)
- Troshichev, O., Hayakawa, H., Matsuoka, A., Mukai, T., & Tsuruda, K. (1996). Cross polar cap diameter and voltage as a function of PC index and interplanetary quantities. *Journal of Geophysical Research*, 101(13), 429–435. <https://doi.org/10.1029/95ja03672>
- Tsutomu, T., & Teruki, M. (1976). Flapping motions of the tail plasma sheet induced by the interplanetary magnetic field variations. *Planetary and Space Science*, 24(2), 147–159. [https://doi.org/10.1016/0032-0633\(76\)90102-1](https://doi.org/10.1016/0032-0633(76)90102-1)
- Volwerk, M., Andre, N., Arridge, C., Jackman, C., Jia, X., Milan, S. E., et al. (2013). Comparative magnetotail flapping: An overview of selected events at Earth, Jupiter and Saturn. *Annales Geophysicae*, 31(5), 817–833. <https://doi.org/10.5194/angeo-31-817-2013>
- Webster, J., Burch, J., Reiff, P., Daou, A., Genestreti, K., Graham, D. B., et al. (2018). Magnetospheric multiscale dayside reconnection electron diffusion region events. *Journal of Geophysical Research: Space Physics*, 123(6), 4858–4878. <https://doi.org/10.1029/2018ja025245>
- Wiltberger, M., Merkin, V., Lyon, J., & Ohtani, S. (2015). High-resolution global magnetohydrodynamic simulation of bursty bulk flows. *Journal of Geophysical Research: Space Physics*, 120(6), 4555–4566. <https://doi.org/10.1002/2015ja021800>

- Wolf, R. A., Harel, M., Spiro, R. W., Voigt, G., Reiff, P. H., & Chen, C. K. (1982). Computer simulation of inner magnetospheric dynamics for the magnetic storm of July 29, 1977. *Journal of Geophysical Research*, 87(A8), 5949–5962. <https://doi.org/10.1029/JA087iA08p05949>
- Wu, C. C., Walker, R., & Dawson, J. M. (1981). A three-dimensional MHD model of the Earth's magnetosphere. *Geophysical Research Letters*, 8(5), 523–526. <https://doi.org/10.1029/gl008i005p00523>
- Zhou, H., Tóth, G., Jia, X., & Chen, Y. (2020). Reconnection-driven dynamics at Ganymede's upstream magnetosphere: 3-D global hall MHD and MHD-epic simulations. *Journal of Geophysical Research: Space Physics*, 125(8), e2020JA028162. <https://doi.org/10.1029/2020ja028162>
- Zhou, H., Tóth, G., Jia, X., Chen, Y., & Markidis, S. (2019). Embedded kinetic simulation of Ganymede's magnetosphere: Improvements and inferences. *Journal of Geophysical Research: Space Physics*, 124(7), 5441–5460. <https://doi.org/10.1029/2019ja026643>